ISSN 0016-7029, Geochemistry International, 2015, Vol. 53, No. 7, pp. 624–647. © Pleiades Publishing, Ltd., 2015.
Original Russian Text © V.Yu. Rusakov, B.N. Ryzhenko, I.A. Roshchina, N.N. Kononkova, V.S. Karpukhina, 2015, published in Geokhimiya, 2015, No. 7, pp. 624–650.

Devonian Ore Clastic Turbidites of the Molodezhnoe Massive Copper Sulfide Deposit, Southern Urals

V. Yu. Rusakov, B. N. Ryzhenko, I. A. Roshchina, N. N. Kononkova, and V. S. Karpukhina

Vernadky Institute of Geochemistry and Analytical Chemistry, Russian Academy of Sciences, ul. Kosygina 19, GSP-1, Moscow, 119991 Russia

e-mail: rusakov@geokhi.ru

Received October 4, 2013; accepted February 4, 2014

Abstract—We present data on the composition of Devonian ore clastic sediments accumulated at the boundaries of the orebodies of the Molodezhnoe massive copper sulfide deposit, Southern Urals. They are interpreted to be accumulated during the synsedimentary and postsedimentary stages. The synsedimentary stage was marked by gravity transport and accumulation of products of the destruction of high-temperature black smoker chimneys. During the postsedimentary stage, the deposits underwent two types of mineralogical and geochemical transformation: (1) infiltration-metasomatic effects of ore-bearing solutions and infiltration effects of seawater causing redistribution of copper and carbonates in the sediments and formation of authigenic minerals (chalcopyrite, siderite, secondary calcite, and apatite and replacement of aluminosilicates by chlorite) and (2) dehydration accompanied by the replacement of iron hydroxides by hematite and amorphous silica by quartz. Temperatures of the postsedimentary alteration were estimated from a fluid inclusion study and thermodynamic computer modeling as 150–250°C and correspond to the metagenesis stage (burial metamorphism). The organic matter composition was characterized by TOC, hydrogen and oxygen indices (HI and OI), and $\delta^{13}C$ values.

Keywords: massive sulfide ores, ore clastic turbidites, mineral and chemical composition, organic matter, stable carbon isotopes, fluid inclusions, massive sulfide deposits, Southern Urals

DOI: 10.1134/S0016702915070095

INTRODUCTION

Clastic ores (ore clastics) have been described in massive sulfide deposits of Canada, for instance, at Buchans, Newfoundland (Binney, 1987), and Rudny Altai at the Nikolaevskoe, Kamyshinskoe, and Ridder–Sokolnoe deposits (Dergachev et al., 1986; Pak and Dergachev, 1993). Moreover, they form an important component of many massive sulfide deposits around the world (Dergachev, 2010) and, according to various authors, may constitute up to 75% of the ore (Spence, 1975).

The genesis of massive sulfide deposits has been discussed in many previous publications (*Massive Sulfide...*, 1950; Betekhtin et al., 1953; Skripchenko, 1972; Borodaevskaya et al., 1979; *Copper Massive...*, 1988, 1992; and others). Wall rocks around the massive orebodies form an important constituent of the sulfide deposit. Earlier studies of ore-bearing hydrothermal sedimentary rocks (Maslennikov, 1999) revealed a number of different facies, such as clastic ores (ore clastic turbidites), gossanites, jasperides, and umbrites, as well as silicites and pelitolites. These sediments form a continuous sequence of lithofacies from a sulfide mound composed largely of ore components of hydrothermal–metasomatic origin to background pelagic sediments (siliceous and/or clayey). Ore clastic turbidites are transitional between metasomatic sulfides (as a product of mechanical disintegration of sulfide structures) and sediments, because they include interbedded sulfide-rich and jasperoid quartz–hematite sediments, e.g., gossanites containing clay minerals. The most detailed description of the textural, structural, and mineralogical features of clastic sulfide lithologies of the Urals was obtained for the Molodezhnoe, Yaman-Kasy, and Saf'yanovka deposits (Safina and Maslennikov, 2008; Maslennikov et al., 2012). The low degree of metamorphism at these deposits (Zaikov and Maslennikov, 1987; Zaikov et al., 1995; Koroteev et al., 1997; Maslennikov, 2006) allows a comparison between the compositions of their sedimentary facies and modern proximal hydrothermal–metasomatic facies.

However, the mechanisms of their accumulation and postdepositional changes are still a matter of debate due to the complexity of reconstruction of postsedimentation history. The origin of any given hydrothermal sedimentary deposit can generally be inferred from subtle features (individual minerals, fluid microinclusions, and chemical composition) that appear to be preserved in the sediments during diagenesis, catagenesis, and epigenesis, whereas the process itself can be rarely observed in nature. This prevents a direct comparison of recent sediments that have not been seriously altered by postdepositional processes and their ancient equivalents, which underwent multiple mineral and chemical

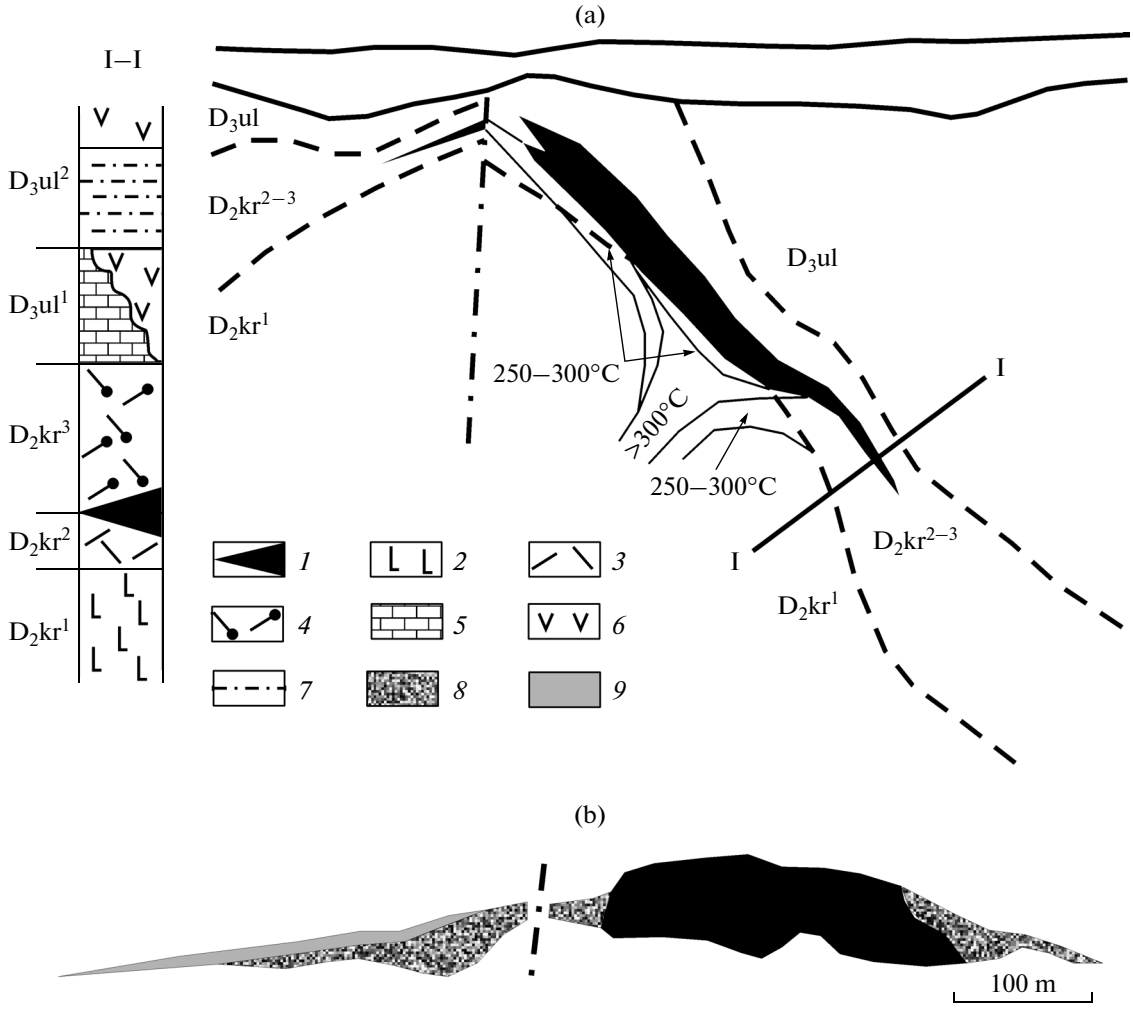

Fig. 1. Study area, Molodezhnoe deposit. (a) Position of the orebody, formation boundaries (ul—Ulutau, kr—Karamalytash), and thermal field in a cross-section view (Baranov, 1987); (I–I)—vertical section of volcanosedimentary sequences (Zaykov et al., 1995): (*1*) copper–zinc massive sulfide ore; (*2–4*) Karamalytash Formation rocks: (*2*) basalt, (*3*) lava and volcanomictic rhyodacite, and (*4*) coarse- to fine-porphyritic rhyolite and dacite; (*5–7*) Ulutau Formation rocks: (*5*) limestone, (*6*) andesite, and (*7*) siltstone and sandstone. (b) Schematic internal structure of the orebody and hydrothermal–sedimentary rocks (Maslennikov, 2006): (*8*) clastic ore and (*9*) Si–Fe metasediments (gossanites).

transformations. A further complexity arises from the processes related to the ascent of reducing hydrothermal solutions through proximal hydrothermal–metasomatic sedimentary facies (infiltration metasomatism) and the downward inflow of oxidizing seawater (infiltration). Grainites deposited by a grain flow, the present-day equivalents of the Devonian ore clastic turbidites, were used to reconstruct the conditions of their formation. The grainites of hydrothermal fields in the Atlantic Ocean are Holocene–Pleistocene ore clastic turbidites, which were formed in a similar environment by the destruction of high-temperature black smoker sulfide chimneys. They were discovered in the proximal hydrothermal sedimentary units of the Semenov ore cluster located at 13°30′ N of the Mid-Atlantic Ridge (MAR) during cruise 32 of the R/V *Professor Ligachev* in 2009 (Beltenev et al., 2007, 2009a, 2009b) and were first described by Rusakov et al. (2013). A comparison of these turbidites with their Devonian equivalents is the focus of this study.

Study Area

The Molodezhnoe deposit lies within the Uzelga massive sulfide ore field, which is located in the Magnitogorsk metallogenic zone. The geologic section consists of the ore-hosting Karamalytash Formation (D_2kr) and the overlying Ulutau Formation (D_3ul) of Middle and Late Devonian age (*Copper Massive...*, 1988; Maslennikov, 1999) (Fig. 1a). The Karamalytash Formation is composed of three distinct units: a footwall basalt unit, an ore-hosting rhyodacite unit, and an overlying rhyolite unit. The deposit is of Eifelian age (Def). The Ulutau Formation is composed of andesites, lime-

stones, and volcanomictic sandstones in the lower part and siltstones and sandstone in the upper part. The deposit comprises four orebodies, two of which contain the main ore reserves. Clastic sulfides are localized on the top and at the flanks of the major orebody (Fig. 1b) and entirely constitute the second orebody. The sheet-like and lenslike orebodies occur at a depth of 80–300 m and have sharp contacts with volcanic rocks. A distinct geochemical aureole at this deposit was observed only locally in the footwall volcanic sequences and represents a high-temperature hydrothermal fluid circulation zone, because it almost completely coincides with the metasomatic aureole (Baranov, 1987). It is poorly developed or absent in the overlying rocks, indicating minor changes in the primary geochemical composition of hydrothermal sedimentary sequences.

Intense volcanic activity in the region was probably favorable for the preservation of most primary textures and sedimentary structures as well as mineral and chemical compositions of turbidites at the Molodezhnoe deposit. The sulfide ores and their host rocks became buried beneath a thick layer of volcanics (rhyodacites, dacites, and basaltic andesites), which led to specific conditions of postsedimentary modification (including lithification) of the sediments in a relatively closed environment, producing only little changes in their mineralogical and geochemical compositions.

Objects of Study

Samples used in this study include clastic sulfides collected from the best explored Molodezhnoe deposit and sandy barite–sulfide rocks from the Vostochnoe deposit of the Semenov ore cluster. Structures and textures, as well as mineral and chemical compositions were analyzed in samples of Pleistocene turbidites (column 32l-362) and three samples of Devonian clastic sulfides provided by the Institute of Mineralogy, Ural Branch of the Russian Academy of Sciences: samples 1 and 2 of proximal facies (Figs. 2, 3) and sample 3 of distal facies (Fig. 4). The lithology, mineralogy, and chemical compositions of these three samples were first described by Maslennikov et al. (2012). The results of our investigations are described below.

METHODS

Structural and textural features of the samples were examined in polished sections and thin sections under a binocular and a petrographic microscope (analyst V.Yu. Rusakov). Based on the preliminary lithological description, individual layers and interlayers were identified in the samples for more detailed mineralogical and chemical analysis. *Mineralogical analysis* was performed using X-ray diffraction, in reflected light on polished sections, and in transmitted light on thin sections (analyst V.Yu. Rusakov), which were prepared for microinclusion studies. Finer grains were studied in the polished thin sections at the Vernadsky Institute of Geochemistry and Analytical Chemistry, Russian Academy of Sciences, using a Camebax SX-100 scanning electron microscope equipped with an analytical system for the determination of the chemical compositions of individual grains and 2D X-ray elemental mapping of selected areas in a thin section (analysts N.N. Kononkova and V.Yu. Rusakov). The composition of clay minerals was determined at the Geological Institute, Russian Academy of Sciences.

The chemical compositions of selected areas cut from the samples were determined at the Vernadsky Institute of Geochemistry and Analytical Chemistry, Russian Academy of Sciences, using X-ray fluorescence (XRF), which is based on the measurement of the intensity of characteristic radiation emitted from the atoms of elements present in the sample. The analyses were performed with an AXIOS Advanced PANalytical B.V. (Holland) spectrometer equipped with an X-ray source with a rhodium anode. A suite of 36 reference materials including bottom sediments, soils, and rocks (SDO, SGHM, SGH, SCR, SDPS, etc.) was used as standards for the construction of calibration curves and quantitative determination of the concentrations of 20 elements (Na, Mg, Al, Si, P, K, Ca, Ti, Mn, Fe, S, V, Co, Cu, Zn, As, Sr, Zr, Ba, and Pb) (Table 1). The analyses were conducted under the guidance of I.A. Roshchina.

The proportions of minerals in the samples were calculated from the chemical analyses of rocks and minerals. Based on the data on mineral composition, the content of each mineral was calculated from the content of the component elements using a special software. The calculation results are given in Table 2.

The homogenization temperatures of **fluid inclusions** in ores and wall rocks (volcanic and sedimentary) were measured in polished thin sections (analyst V.S. Karpukhina) (Table 3).

The composition of **organic matter** (contents of organic carbon and other organic materials) was determined by Rock-Eval pyrolysis using a Rock-Eval 6 instrument. The method is based on programmed heating of a small amount of rock (100 mg) in an inert atmosphere (helium or nitrogen) in a temperature range of 100–850°C to quantitatively determine the contents of hydrocarbons (CH) and oxygen-containing compounds (CO_2) released during the cracking of insoluble organic matter (kerogen) contained in the sample. The total organic carbon content (TOC) was measured by oxidation under an air flow. The hydrogen (HI = mg HC/g TOC) and oxygen (OI = mg CO_2/g TOC) indices were used to identify oxygen-containing organic compounds (Table 4). In addition, the $\delta^{13}C$ value of organic matter was determined in sample 1 using a DELTA-plus Finnigan mass spectrometer (USA) at the Vernadsky Institute of Geochemistry and Analytical Chemistry, Russian Academy of Sciences (analyst V.P. Strizhev). All samples were pretreated with a 2% HCl solution to remove carbonate material. Similar measurements were performed for sample 3 without acid pretreatment (organic + inorganic carbon).

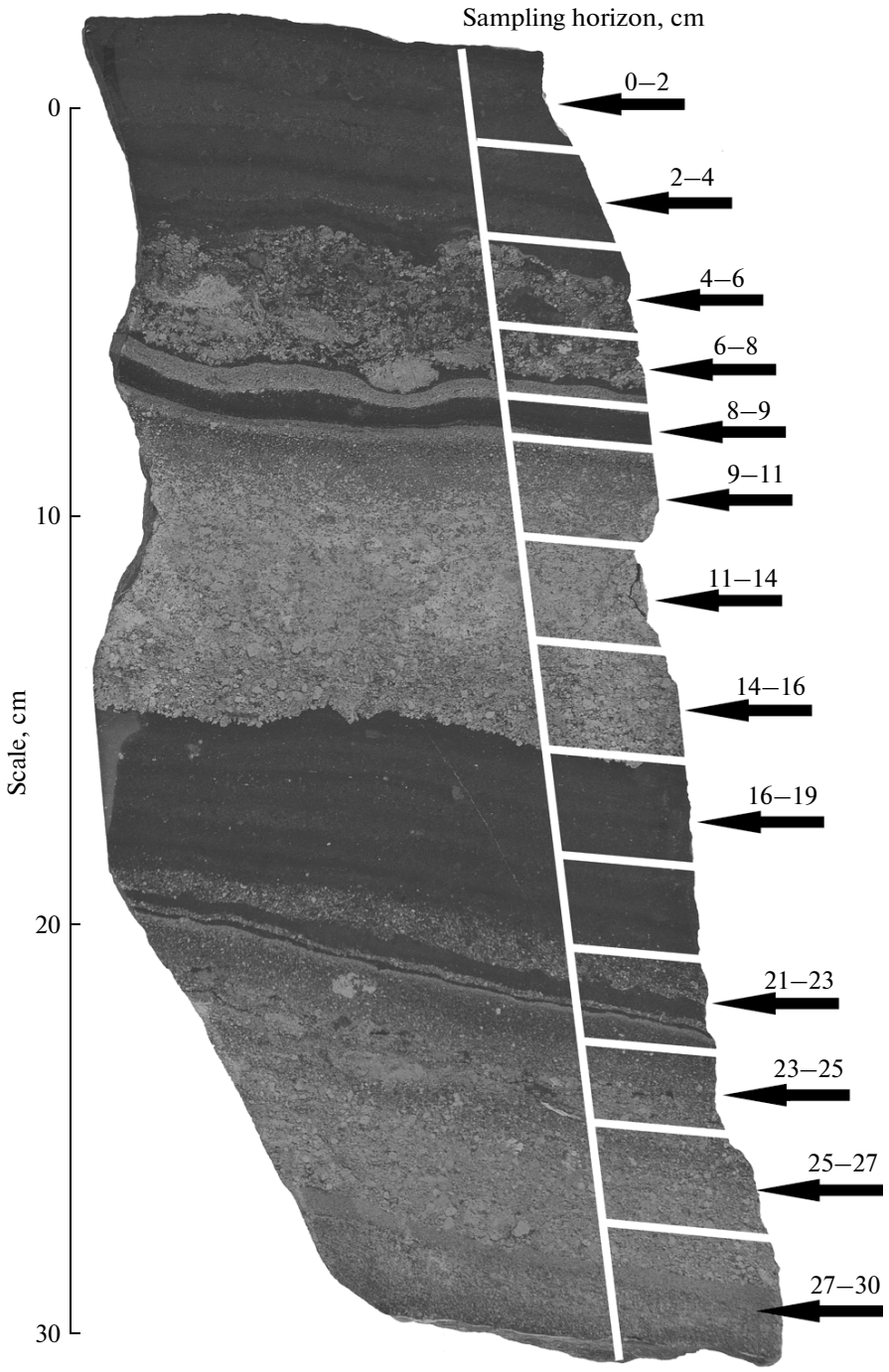

Fig. 2. Proximal ore clastic turbidite (sample 1). Molodezhnoe massive copper sulfide deposit (Southern Urals).

MATERIALS

Holocene–Pleistocene Turbidites

Column 32l-362 (13°30.361′ N, 44°53.186′ E, 2857 m water depth) is 45 cm long. Seven intervals were recognized in this column on the basis of color, texture, and structure. The upper interval (0–2 cm) is composed of brown fluidized iron hydroxide–sulfide–barite mud, containing rare foraminiferal tests and 6 wt % biogenic carbonates. Interval 2–7 cm consists of brownish, more compact, but still soft and wet iron hydroxide–barite sediments and can be distinguished from the above interval by the presence of bioturbation spots. Late Pleistocene age is indicated for both intervals (0–7 cm) by the foraminiferal assemblages. Interval 7–13 cm is composed of yellowish to orange carbonate-free sediments. The mineral composition of the layers was not determined. Interval 13–21 cm is composed of grey

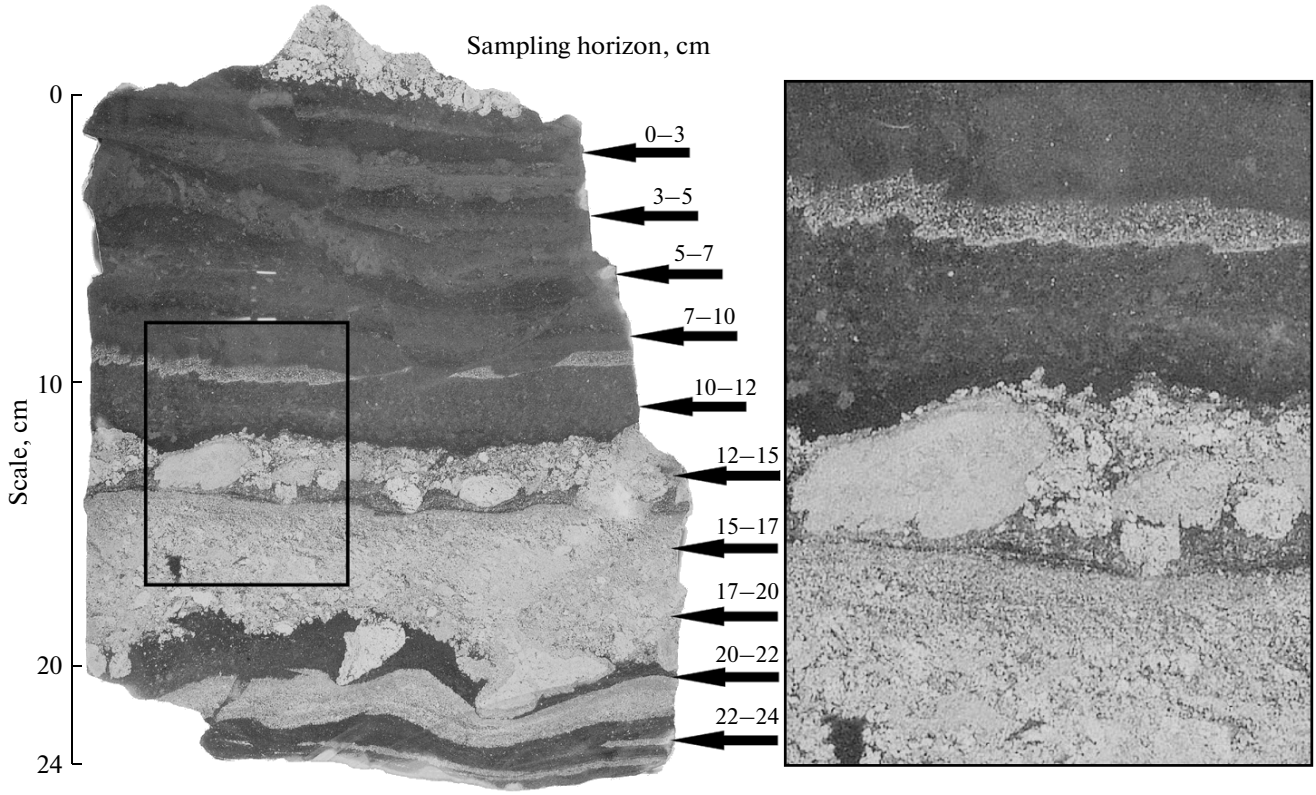

Fig. 3. Proximal ore clastic turbidite (sample 2). Molodezhnoe massive copper sulfide deposit (Southern Urals). Part of the turbidite (rectangle in the left image) is shown in the inset at a higher magnification.

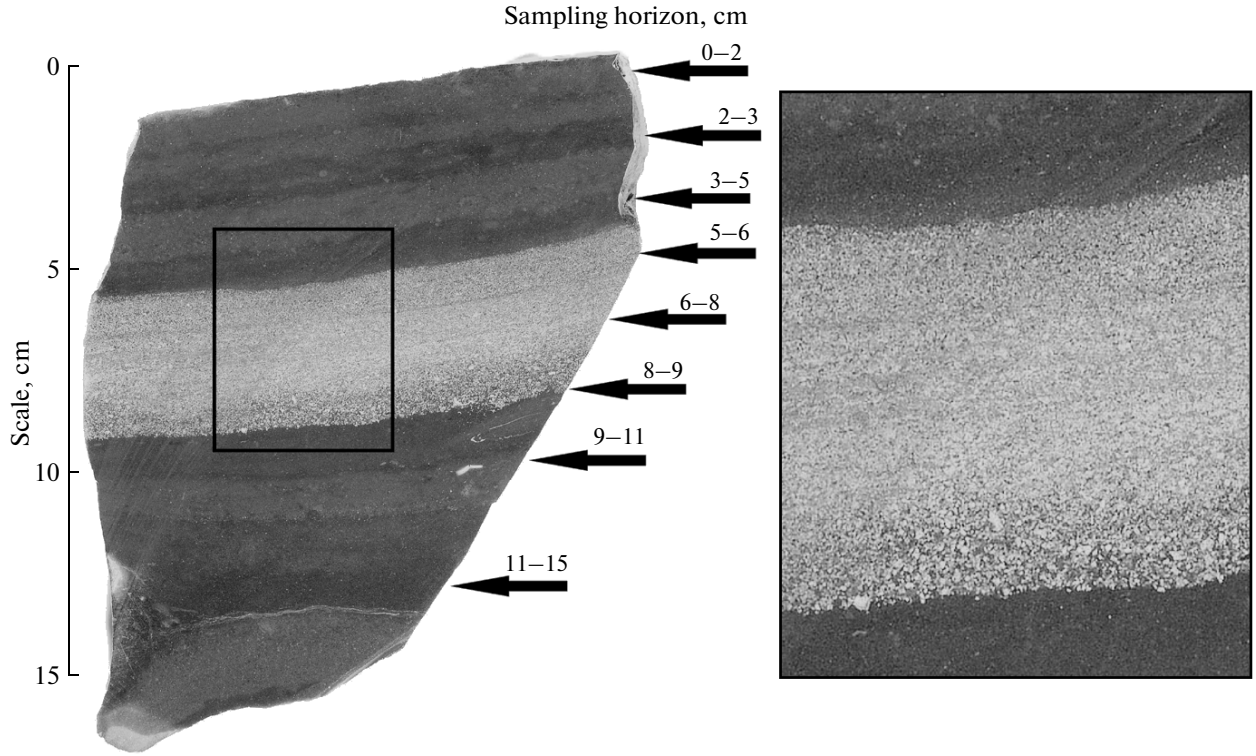

Fig. 4. Distal ore clastic turbidite (sample 3). Molodezhnoe massive copper sulfide deposit (Southern Urals). Part of the turbidite (rectangle in the left image) is shown in the inset at a higher magnification.

Table 1. XRF data for samples, wt %

Sample	Horizon, cm	Na	Mg	Al	Si	P	S	Ca	Ti	Mn	Fe	Cu	Zn	As	Sr	Ba	Pb	l.o.i.
Column 32l-362	0–2	0.36	0.2	1.06	3.51	0.093	21.44	2.29	n.d.	n.d.	27.25	4.12	0.233	n.d.	0.292	25.34	n.d.	5.98
	5–6	0.38	0.26	1.09	4.62	0.122	6.97	1.83	n.d.	n.d.	40.73	3.54	0.275	n.d.	n.d.	21.18	n.d.	11.32
	15–16	0.42	0.031	0.16	0.48	b.d.l.	36.16	0.073	n.d.	n.d.	13.91	4.143	1.37	n.d.	0.209	23.11	n.d.	13.46
	44–45	0.39	0.11	0.57	2.77	0.089	0.87	0.18	n.d.	n.d.	39.04	1.42	0.34	n.d.	0.268	19.02	0.169	12.12
1	0–2	0.007	0.886	3.775	11.608	0.506	5.46	1.186	0.107	0.17	48.84	0.002	0.134	0.147	0.211	10.27	n.d.	2.8
	2–4	b.d.l.	0.627	3.262	10.964	0.33	7.62	0.586	0.154	0.146	47.5	0.013	0.118	0.068	0.285	15.38	0.082	2.37
	4–6	0.007	0.127	1.811	11.608	0.115	24.44	0.121	n.d.	0.09	40.94	0.131	0.14	0.201	0.327	10.37	0.46	0.96
	6–8	b.d.l.	0.428	2.256	10.525	0.492	23.54	1.079	n.d.	0.13	32.39	3.023	0.347	0.18	0.24	14.35	0.231	1.12
	8–9	0.007	0.645	2.854	7.747	0.31	12.6	0.522	n.d.	0.148	37.82	0.058	0.089	0.168	0.38	26.32	n.d.	2.3
	9–11	b.d.l.	0.001	0.609	13.666	0.008	25.33	3.566	n.d.	0.1	19	1.33	0.449	0.065	0.199	13.21	0.294	12.36
	11–14	0.007	b.d.l.	0.079	4.16	b.d.l.	32.71	1.68	n.d.	0.006	23.37	6.608	0.008	0.121	0.117	9.98	0.137	17.85
	14–16	b.d.l.	b.d.l.	0.349	4.746	0.056	32.38	0.2	0.204	b.d.l.	25.42	2.65	0.032	0.158	0.108	8.9	0.121	21.71
	16–19	0.007	0.772	2.812	7.174	1.122	8.44	2.551	n.d.	0.17	44.62	0.039	0.122	0.161	0.245	16.72	n.d.	2.63
	21–23	b.d.l.	0.253	1.795	3.784	0.192	19.57	0.25	n.d.	0.101	39.75	0.191	0.055	0.106	0.311	21.02	0.225	8.11
	23–25	0.007	b.d.l.	0.916	13.634	b.d.l.	24.58	0.007	n.d.	b.d.l.	17	0.18	0.032	0.081	0.316	23.9	0.192	10.53
	25–27	0.007	b.d.l.	0.312	4.326	b.d.l.	32.68	0.019	n.d.	0.006	24.49	1.017	0.037	0.153	0.149	12.74	0.109	20.95
	27–30	0.007	b.d.l.	0.265	2.943	0.001	33.27	b.d.l.	n.d.	0.006	24.53	2.029	0.038	0.154	0.159	14.042	0.098	20.47
2	0–3	b.d.l.	3.860	7.630	14.330	1.248	1.226	1.910	0.322	0.246	60.00	0.172	0.213	0.057	0.092	8.522	n.d.	n.d.
	3–5	0.140	3.510	7.380	11.690	1.231	1.146	1.940	0.331	0.187	63.30	0.010	0.211	0.042	0.101	8.704	n.d.	n.d.
	5–7	0.107	2.990	6.190	8.160	1.095	1.740	1.603	0.199	0.181	66.31	0.018	0.211	b.d.l.	0.135	11.020	n.d.	n.d.
	7–10	b.d.l.	2.840	5.560	8.090	1.029	2.580	1.480	0.144	0.127	62.76	0.259	0.145	0.098	0.161	14.790	n.d.	n.d.
	10–12	b.d.l.	2.290	4.760	6.290	1.098	2.561	1.571	0.133	0.240	66.00	0.391	0.156	0.048	0.146	14.300	n.d.	n.d.
	12–15	b.d.l.	0.890	1.960	4.810	0.028	32.980	0.073	b.d.l.	0.085	42.38	5.355	0.067	0.140	0.182	11.061	n.d.	n.d.
	15–17	0.080	0.310	0.640	5.920	0.023	35.220	b.d.l.	b.d.l.	b.d.l.	38.70	9.674	0.031	0.134	0.120	8.204	n.d.	n.d.
	17–20	0.200	b.d.l.	1.080	2.490	b.d.l.	35.030	0.273	b.d.l.	b.d.l.	44.00	1.153	0.166	0.130	0.247	15.300	n.d.	n.d.
	20–22	0.144	1.770	4.000	6.980	0.707	26.010	1.450	0.196	0.155	45.87	2.002	0.166	0.126	0.151	10.320	n.d.	n.d.
	22–24	b.d.l.	4.570	11.160	14.300	1.920	7.510	3.370	0.610	0.372	51.10	1.115	0.455	0.188	0.048	2.520	n.d.	n.d.
3*	0–2	0.104–0.141	2.038–2.237	6.185–6.482	19.574–20.846	0.293–0.331	0.42–0.568	0.668–0.729	0.141–0.157	0.016–0.049	32.716–33.386	0.053–0.083	0.18–0.183	0.037–0.056	0.019–0.028	1.422–1.751	n.d.	n.d.
		0.123	2.165	6.334	20.178	0.312	0.499	0.706	0.149	0.031	33.051	0.072	0.182	0.047	0.024	1.538	–	–
	2–3	n.d.	2.038–2.15	5.642–5.915	19.574–20.638	0.331–0.398	0.241–0.508	0.722–0.849	0.157–0.337	0.028–0.029	32.716–33.297	0.044–0.053	0.178–0.183	0.037	0.019–0.026	1.44–1.908	n.d.	n.d.
		–	2.094	5.779	20.106	0.365	0.375	0.786	0.247	0.029	33.007	0.049	0.181	–	0.023	1.674	–	–
	3–5	0.075–0.082	1.910–2.136	4.98–5.294	12.645–17.757	0.307–0.364	0.59–0.652	0.715–0.896	0.093–0.133	0.03–0.031	40.923–41.531	0.064–0.086	0.215	0.058	0.039–0.048	2.602–3.688	0.08	n.d.
		0.079	2.023	5.137	14.681	0.326	0.63	0.806	0.113	0.031	41.227	0.075	–	–	0.044	3.145	–	–
	5–6	0.074–0.111	1.208–2.52	2.799–6.14	6.008–6.061	0.084–0.101	10.241–11.256	0.226–0.733	0.056–0.26	0.067–0.105	33.292–35.615	0.243–2.306	0.209	b.d.l.	0.057–0.059	3.584–4.045	0.098	n.d.
		0.093	1.864	4.47	6.035	0.093	10.749	0.48	0.158	0.086	34.454	1.275	–	–	0.058	3.815	–	–
	6–8	0.046–0.122	1.107–1.208	0.86–1.045	7.912–8.635	0.026–0.039	8.735–10.87	7.583–13.261	b.d.l.	0.033–0.068	20.905–21.414	6.072–7.807	b.d.l.	b.d.l.	0.121–0.135	3.504–7.188	0.05	n.d.
		0.084	1.141	0.953	8.274	0.033	9.8	9.985	–	0.046	21.16	6.94	–	–	0.128	5.346	–	–
	8–9	0.074–0.112	0.522–1.761	1.112–1.625	7.478–17.406	0.075–0.307	9.732–11.758	0.693–0.968	0.138	0.008	27.022–28.099	2.306–2.912	b.d.l.	b.d.l.	0.163–0.198	10.629–11.536	n.d.	n.d.
		0.093	1.142	1.369	12.442	0.191	10.745	0.831	–	–	27.561	2.609	–	–	0.181	11.083	–	–
	9–11	0.074–0.122	1.598–1.761	4.252	17.406–19.985	0.199–0.307	n.d.	0.693	0.138–0.191	0.039–0.057	28.099–28.254	0.114–0.118	b.d.l.	b.d.l.	0.194	10.647–11.536	n.d.	n.d.
		0.098	1.68	–	18.696	0.253	–	–	0.165	0.048	28.177	0.116	–	–	–	11.092	–	–
	11–15	0.178	1.912	5.729	20.534	0.897	1.386	2.308	0.294	0.115	23.23	0.074	0.027	0.037	0.196	9.9	n.d.	n.d.
CSO**	–	b.d.l.	b.d.l.	0.381	0.682	0.010	18.628	0.050	b.d.l.	b.d.l.	18.928	21.810	2.220	0.110	b.d.l.	0.085	n.d.	n.d.

b.d.l. denotes below the detection limit.
n.d. denotes no data.

* For sample 3, the upper figures show the interval of values, and the lower figure is the mean value.

** CSO is copper massive sulfide ore.

Table 2. Quantitative mineralogy of samples determined from microscopic examination and chemical analysis, wt %

Sample	Horizon, cm	$Fe_2O_3/HFeO_2$*	SiO_2/SiO_2amorph.*	Aluminosilicates	$CaCO_3$	Apatite	$BaSO_4$	FeS_2	$CuFeS_2$	ZnS	Mineral type of sediments	Lithotype (LT)
Column 321-362	0–2	18	8	1	6	0	40	15	7	–	Iron hydroxide–sulfide–barite (IHSB)	Metalliferous sediment
	5–6	36	10	1	4.6	0	36	7.4	2	–	Iron hydroxide–barite (IHB)	
	15–16	0	1	1	0	0	39	47	12	–	Barite–sulfide sand (BSS)	Fine-grained clastic ore
	44–45	55	6	1	0	0	32	1	5	–	Barite–iron hydroxide (BIH)	Metalliferous sediment
1	0–2	62.18	18.22	5.66	0	2.82	10.27	1	0.01	–	Barite–iron oxide (BIO)	Gossanite
	2–4	60.09	17.21	4.89	0	1.58	15.38	1	0.04	–	Barite–iron oxide (BIO)	
	4–6	14	11.91	2.72	0	0.3	10.37	60.32	0.38	–	Barite–iron oxide–sulfide (BIOS)	Coarse-grained
	6–8	12	11.66	3.38	0	2.7	14.35	47.20	8.71	–	Iron oxide–barite–sulfide (IOBS)	clastic ore
	8–9	54.08	12.16	4.28	0	1.44	26.32	1.55	0.17	–	Barite–iron oxide (BIO)	Gossanite
	9–11	0	21.45	0.91	8.92	0	13.21	51.68	3.83	–	Barite–sulfide (BS)	Mixture of fine-
	11–14	0	6.53	0.12	+	4	9.98	60.14	19.03	–	Barite–sulfide (BS)	and coarse-grained
	14–16	0	7.45	0.52	+	1.39	8.90	74.11	7.63	–	Barite–sulfide (BS)	clastic ore
	16–19	61.55	11.26	4.22	0	6.14	16.72	0	0.11	–	Barite–iron oxide (BIO)	Gossanite
	21–23	30.31	5.94	2.69	0	0.79	21.02	38.70	0.55	–	Barite–iron oxide–sulfide (BIOS)	Fine-grained clastic ore
	23–25	1	21.40	1.37	+	0.01	23.00	52.70	0.52	–	Barite–sulfide (BS)	Mixture of fine-
	25–27	0	6.79	0.47	+	0.03	12.74	77.04	2.93	–	Barite–sulfide (BS)	and coarse-grained
	27–30	0	4.62	0.40	+	0.00	14.04	75.08	5.84	–	Barite–sulfide (BS)	clastic ore
2	0–3	50.71	21.96	16.93	0	3.80	5.06	1.08	0.28	0.18	Iron oxide (IO)	Gossanite
	3–5	54.86	18.13	15.67	0	3.50	7.47	0.17	0.01	0.18	Iron oxide (IO)	
	5–7	59.70	13.00	13.41	0	3.10	10.43	0.14	0.03	0.19	Barite–iron oxide (BIO)	
	7–10	56.80	12.98	12.20	0	3.00	14.35	0	0.46	0.13	Barite–iron oxide (BIO)	Fine-grained clastic ore
	10–12	61.00	10.23	10.50	0	2.50	14.07	0	0.71	0.15	Barite–iron oxide (BIO)	Gossanite
	12–15	16.65	9.07	5.02	0.07	0	15.12	41.55	12.44	0.08	Barite–iron oxide–sulfide (BIOS)	Coarse-grained clastic ore
	15–17	10.16	11.41	11.84	0	1.11	11.68	40.27	23.49	0.04	Iron oxide–barite–sulfide (IOBS)	Mixture of fine-
	17–20	17.38	4.75	3.19	0	0	21.17	50.41	2.72	0.08	Iron oxide–barite–sulfide (IOBS)	and coarse-grained
	20–22	24.70	12.38	9.76	0	2.7	12.66	33.45	4.19	0.18	*****	clastic ore
	22–24	37.69	21.63	22.36	0	6	2.38	7.09	2.48	0.37	Iron oxide (IO)	Fine-grained clastic ore
3	0–2	47.00	27.76	20.35	0	1.73	2.42	0.51	0.23		Iron oxide (IO)	Gossanite
	2–3	44.59	31.57	19.46	0	1.78	2.45	0	0.15		Iron oxide (IO)	
	3–5	58.50	15.46	17.50	0	2.09	6.27	0	0.18		Iron oxide (IO)	
	5–6	37.13	9.43	9.21	0	0.55	6.09	30.95	6.64		*****	Fine-grained
	6–8	19.44	13.55	3.44	18.56	0	12.22	15.28	17.51	–	Barite–iron oxide–sulfide (BIOS)	clastic ore
	8–9	24.86	11.74	5.35	0	2.24	18.07	29.43	8.31	–	Barite–iron oxide–sulfide (BIOS)	
	9–11	33.28	31.37	14.86	0	2.06	18.01	0	0.33	–	Barite–iron oxide (BIO)	Gossanite
	11–15	26.59	32.23	18.85	0	5.29	16.83	0	0.21		Barite–iron oxide (BIO)	
CSO	–	0	1.07	1.25	0	0	0.14	29.66	62.81	4.97	Sulfide	Copper massive sulfide ore

* Holocene–Pleistocene sediments.

* Mineral type of sediments was distinguished based on their major mineral (>10 wt %) contents ignoring silicates, aluminosilicates, and carbonates.

***** Boundary horizon between layers of different lithotypes.

CSO denotes copper massive sulfide ore.

Table 3. Homogenization temperatures (°C) of fluid inclusions in hydrothermal minerals from the wall rocks and ores of the Molodezhnoe copper massive sulfide deposit (Southern Urals) (Karpukhina et al., 2013)

Volcanic wall rock	Massive ore	Colloform and banded ore	Recrystallized ore	Recrystallized cross-cutting ore veins
135–270	150–325	150–210	190–300	265–325

Table 4. Organic carbon content (wt %), hydrogen index (HI), oxygen index (OI), and carbon isotopic composition ($\delta^{13}C$, ‰) of gossanite and clastic ore layers

Sample no.	LT	C_{org}	HI	OI	OI/HI	$\delta^{13}C$
1	Gossanit	0.02	35	893	26	–26.93
	Clastic ore	0.03	14	305	22	–26.74
3	Gossanit	0.03	199	1075	5	–5.59*
	Clastic ore	0.1	47	289	6	–7.31*

* Without HCl treatment.

barite–sulfide sand in the form of grainite deposited by a grain flow (distal turbidites). The base of this interval contains a 0.5 cm-thick layer of barite–sulfide sand of reddish color (due to fine chalcopyrite grains) admixed with iron–chert aggregates. Interval 21–24 cm consists of brown to orange carbonate-free sediments. The mineral composition of the layer was not determined. Interval 24–31 cm consists of grey barite–sulfide sand similar to that in interval 13–21 cm. The base of this interval also contains a 1 cm-thick layer with an admixture of iron–chert aggregates and fine chalcopyrite grains. Interval 31–45 cm consists of carbonate-free barite–iron hydroxide sediments, brown to orange in color. The topmost 9 cm have a bioturbated texture. Bioturbation spots constitute 50% of this interval, rendering the sediment a grey color.

Devonian Turbidites

All samples are similar in their structural features and consist of horizontal quartz–hematite layers interbedded with clastic sulfide ores of pyrite and pyrite–chalcopyrite compositions. Based on mineralogical and textural observations, these layers can be divided into three lithotypes: jasperoid quartz–hematite layers (gossanite, a lithified product of ore-bearing sediments) and fine- and coarse-grained clastic ore-bearing turbidity current deposits (Table 2), which are referred to as clastic ore sediments based on the presence of layers of ore clasts. The structure of the vertical section of these sediments is defined by their transitional lithofacies position between a massive orebody (of metasomatic origin) and iron-oxide deposits (of hydrothermal–sedimentary origin). Such ore clastics are sometimes referred to as banded ores because of the interlayering of ores (sulfides) and quartz–hematite rocks. They can be divided into proximal and distal facies (rhythmites) based on the clast size and lithodynamic characteristics. For example, sulfide ores containing gravel-sized or larger ore clasts are classified as proximal facies deposited close to the source of ore materials, and smaller-sized (mostly sand-sized) sulfides are assigned to distal facies deposited at a distance from the massive orebody. The products of destruction of high-temperature black smoker sulfide chimneys transported by gravity (turbidity) currents to adjacent seafloor topographic lows are the main source of ore material.

Sample 1 can be conditionally subdivided into five intervals. The upper interval (0–4 cm) is composed of jasperoid quartz–hematite aggregates with a microbreccia-like texture (Fig. 2), which can be classified as gossanite based on mineralogical and textural observations. This interval consists of interbedded ruddy and deep red layers. Light-colored (ruddy) layers are dominated by hematite, and darker (deep red) layers are rich in quartz. The contacts between these layers (1 cm-thick and more) are sharp, although erratic inclusions of one layer in the other are present, indicating horizontal transport of the sediment during deposition. Disseminated fine grains of pyrite and, more rarely, chalcopyrite and sphalerite are found at the base of this interval. The contact with the underlying interval is obscure and strongly brecciated in places.

Interval 4–8 cm consists of coarse-grained clastic ores represented by fragments of sulfide grains mixed with quartz and hematite grains. The uppermost part is dominated by fine gravel-sized ore clasts, which coarsen toward the base of the layer, where ore fragments up to 1 cm in size are present. The base of this interval contains a 0.5 cm-thick layer of well-sorted sand-sized sulfide grains. The interval displays grain-size grading and no mixing between the upper coarse-grained and lower fine-grained clastic sulfides. Moreover, the upper and lower parts are separated from one another by a thin (2–3 mm) quartz–hematite layer, which probably served a glide horizon of the upper tur-

bidite. Load casts below dense sulfide grains (Fig. 2) indicate that the primary iron hydroxide-bearing sediments were water-rich and plastic.

Interval 9–16 cm represents a mixture of fine- and coarse-grained clastic sulfides with a distinct gradational structure. It is separated from the above interval by a distinct undulated quartz–hematite layer at 8–9 cm. The interval is characterized by increasing amounts of coarse-grained sulfides toward its base, and the grain size increases from sand to gravel. The upper part of the interval contains a carbonate cement, and chalcopyrite cementing pyrite clasts becomes more abundant in the central part.

Interval 16–(21–23) cm consists of quartz–hematite sediments. Its thickness increases from left to right in Fig. 2. The textures, structures, and mineralogy of this interval are similar to those of interval 0–4 cm. Its base contains two layers of fine-grained clastic sulfides, ranging in thickness from 0.5–1 cm (upper) to about 2–3 mm (lower).

The lowermost part of this column at (21–23)–30 cm is composed of ore clastic sediments consisting of poorly sorted, coarse, gravel-sized sulfides with numerous erratic quartz–hematite inclusions less than 0.5 cm in size. The sediments of this interval show less developed grain-size grading compared with intervals 4–8 cm and 9–16 cm and are hereafter referred to as poorly graded clastic sulfides.

The structural and textural features of *sample 2* are similar to those of sample 1. Based on mineralogical and textural observations, this sample can be divided into the upper (0–12 cm) interval of quartz–hematite composition and the lower (12–22 cm) interval of clastic sulfides (Fig. 3).

The upper (0–12 cm) interval displays laminated and brecciated sedimentary textures. Some layers are disturbed by pinching out. A horizon at 7–10 cm is dissected by fine-grained clastic sulfides with traces of postsedimentary folding (see the upper part of a higher magnification image in Fig. 3).

The lower (12–22 cm) interval can be conditionally divided into three distinct layers: upper (12–15 cm), middle (15–20 cm), and lower (20–22 cm), consisting of coarse-grained, poorly graded, and fine-grained clastic sulfides, respectively. Texturally, it is similar to interval 4–8 cm of sample 1, but differs from it in that a layer of poorly graded clastic sulfides occurs between the layers of coarse- and fine-grained sulfide ores.

The progressive grain-size grading in the turbidites probably took place during their transport by gravity flows along the seafloor. As the turbidites move downslope, the coarsest sulfide grains settle out first (forming coarse-grained clastic ore deposits), which results in a progressive downslope fining and deposition of fine-grained clastic ore sediments. The underlying fluidized and plastic layer of iron hydroxide sediments serves as a glide plane for the turbidite. Large and heavy clasts tend to fall out of the flow and be trapped in this viscous layer. An isolated large sulfide clast surrounded by quartz–hematite sediments is clearly seen at the base of the turbidite at 20–22 cm (Fig. 3).

Sample 3. The absence of large sulfide clasts and more quiet hydrodynamic conditions during the deposition of the distal (fine-grained) clastic sulfides promoted the development of distinct horizontal layering, which enabled a more detailed structural and textural characterization of the vertical section. As noted above, distal fine-grained sulfide clastics are sometimes referred to as rhythmites to emphasize a succession of repeated layers in the vertical section, in which each layer has a similar vertical pattern. Structurally and texturally, this sample bears a notable resemblance to the sandy barite–sulfide layers in column 32l-362.

The sample can be conditionally divided into three layers with jasperoid quartz–hematite sediments in the upper (0–5 cm) and lower (9–15 cm) layers and sandy (fine-grained) clastic sulfides in the middle (5–9 cm) layer (Fig. 4). Similar to the above samples, the quartz–hematite sediment exhibit horizontal layering, with light (ruddy) and dark (deep red) layers less than 1 cm thick. The hematite and quartz grains are isolated from each other and often have no distinct boundaries, with the exception of detrital quartz grains embedded in a fine-grained matrix of quartz and hematite. Generally, the texture of hematite is fine-grained, with very finely disseminated sulfide minerals in places. The upper layer contains thin barite veins cutting across the horizontal layering in different directions. The lower quartz–hematite layer is richer in barite, which occurs as isolated grains.

The clastic sulfide layer displays a fine-grained texture and well-developed grain-size grading (smaller sulfide grains coarsen from top to bottom in the layer) (Fig. 4). It is well seen that this layer contains isolated large grains of quartz and hematite, from several millimeters to a few tens of millimeters in size, which are probably erratic inclusions from the other layers. Examination under high magnification shows individual cubic crystals and massive grains of pyrite with decomposition textures and later chalcopyrite veinlets. The middle layer of clastic sulfides has a carbonate cement and is lighter in color. Close to the base of this layer, the spaces between pyrite grains are almost completely filled by chalcopyrite, which gives this layer a golden shade. As noted above, similar interlayers containing abundant grains of chalcopyrite are also present at the base of the barite–sulfide turbidites in column 32l-362. Therefore, it can be concluded that calcite and chalcopyrite were precipitated within the turbidite layer and at its base, respectively, at a postsedimentary stage of deposit formation.

As noted above, the **mineralogical composition** of samples was determined by XRD and using binocular and petrographic microscopes and a scanning electron microscope. The contents of major ore minerals were calculated from the whole-rock chemical data. The

results for individual layers and interlayers are given in Table 2. It can be seen that the distinguished mineral types of sediments (MTS) are more informative compared to the lithotypes that were identified based on mineralogical and textural observations. For example, based on the contents of major minerals, we distinguished two types of gossanites: iron oxide (IO) and barite–iron oxide (BIO), and three types of sulfide clastics: barite–iron oxide–sulfide (BIOS), iron oxide–barite–sulfide (IOBS), and barite–sulfide (BS). The mineral composition will be described in detail separately for each type of sediments.

IO. The main minerals in this type of sediments are quartz and hematite (sometimes clay minerals), and the minor phases are clay minerals (ferromagnesian aluminosilicates, chlorites) and barite (Table 2). Pyrite, chalcopyrite, sphalerite, and apatite (rarely, Cu sulfosalts and tellurides) are accessory minerals. As noted above, these sediments form horizontal layers with strong vertical variations in major mineral contents. Microscopic examination reveals vague boundaries between relatively large quartz–hematite and hematite–quartz aggregates. Thin barite veinlets are locally present along the grain boundaries.

Higher magnification SEM images show that hematite, quartz, and ferromagnesian aluminosilicate (chlorite) grains are intergrown with each other and have vague boundaries. The impressions of shells replaced with hematite are present. Hematitization of foraminiferal tests is typical of present-day hydrothermal sedimentary facies of the Central Atlantic due to the dissolution of biogenic carbonate by reducing and acid ore-bearing solutions. The tests are often filled with chlorite and quartz and are overgrown by a chlorite-group ferromagnesian aluminosilicate. This clay mineral contains visible segregations of secondary quartz, which, like hematite, may replace carbonates. Fragments of calcium carbonate shells are also common. However, in the IO- and BIO-type aggregates, calcium is commonly hosted by apatite crystals.

The primary quartz–hematite rock was probably a mixture of iron hydroxides and amorphous silica with minor amounts of clay minerals. It was shown that in the TAG, Krasnov, and Semenov fields (Gurvich, 1998; Rusakov et al., 2011, 2012, 2013), the main components are Fe–Si and Si–Fe phases hardly identifiable in XRD patterns, as well as clay minerals (e.g., nontronite) sometimes containing native sulfur and sulfide minerals. It should be noted that, according to deep sea drilling data, nontronite is absent in ancient metalliferous sediments. It seems likely that nonotronite can only form in a narrow range of Eh and pH and is replaced by another mineral or minerals (in our case, chlorite) during diagenesis.

BIO. Unlike the above type, the BIO-type sediments contain higher amounts of barite, which is one of the major minerals (>10 wt %) (Table 2). Barite is present as finely disseminated particles or thin veins in IO and as large grains with clearly identifiable crystals in BIO. The higher barite content generally reflects the interaction between ore-bearing solutions and seawater, because hydrothermal solutions are the main source of Ba, and seawater is a source of sulfate sulfur.

BIOS. The main minerals in this type are sulfides (pyrite and, sometimes, chalcopyrite), hematite, and barite, and the minor minerals are chalcopyrite, sphalerite, calcite, and siderite (Table 2). This type is typical of distal (fine-grained) clastic sulfides, although it was also found in coarse-grained clastic ores (sample 1, layer 4–6 cm and sample 2, layer 12–15 cm). The distribution of grain size and mineral components in the clastic sulfide layer (5–9 cm) of sample 3 has a distinct vertical stratification (Fig. 5). For example, the top of the layer is characterized by the highest pyrite and hematite contents. The content of calcite and chalcopyrite progressively increases with depth. Both minerals form layers that grade into each other. As noted above, chalcopyrite occurs as fracture filling in pyrite, whereas calcite cements clasts. Massive homogeneous chalcopyrite grains at the base of the layer form isolated fine inclusions in a quartz–hematite rock. Quartz grain size also increases from top to bottom in the layer.

IOBS-type sediments are characterized by larger and more massive sulfide clasts and higher barite content compared to the above facies (Table 2). They are typical of proximal turbidites (coarse-grained clastic deposits), but, compared with the distal turbidites, show much lower contents of hematite and clay minerals.

BS-type sediments are characterized by the presence of both coarse clastic and poorly sorted (poorly graded) sulfides. The main mineral is pyrite (rarely chalcopyrite), the minor minerals are barite and chalcopyrite, and calcite occurs in accessory amounts (Table 2). These sediments exhibit little or no grading in grain size, which suggests deposition in the vicinity of the source of ore material (at the base of black smoker chimneys).

Thus, based on the mineralogical and textural observations, the clastic ore facies can be subdivided into three subfacies: poorly graded clastic ores, coarse-grained clastic ores, and fine-grained clastic ores. They form a lithofacies sequence reflecting continuous changes in the lithodynamic conditions of turbidite deposition with distance from a massive orebody to gossanites.

Chemical Composition

Fe–Si–Al. The highest Fe (40–66 wt %), Si (10–20 wt %), and Al (3–10 wt %) contents are characteristic of quartz–hematite layers in gossanites (Fig. 6). The main minerals hosting these elements are hematite (Fe), quartz (Si), and chlorite (Al). However, sample 3 has lower Fe (<40 wt %) and higher Si (>15 wt %) contents compared with similar layers in other samples (Table 1), which may reflect a greater distance from the

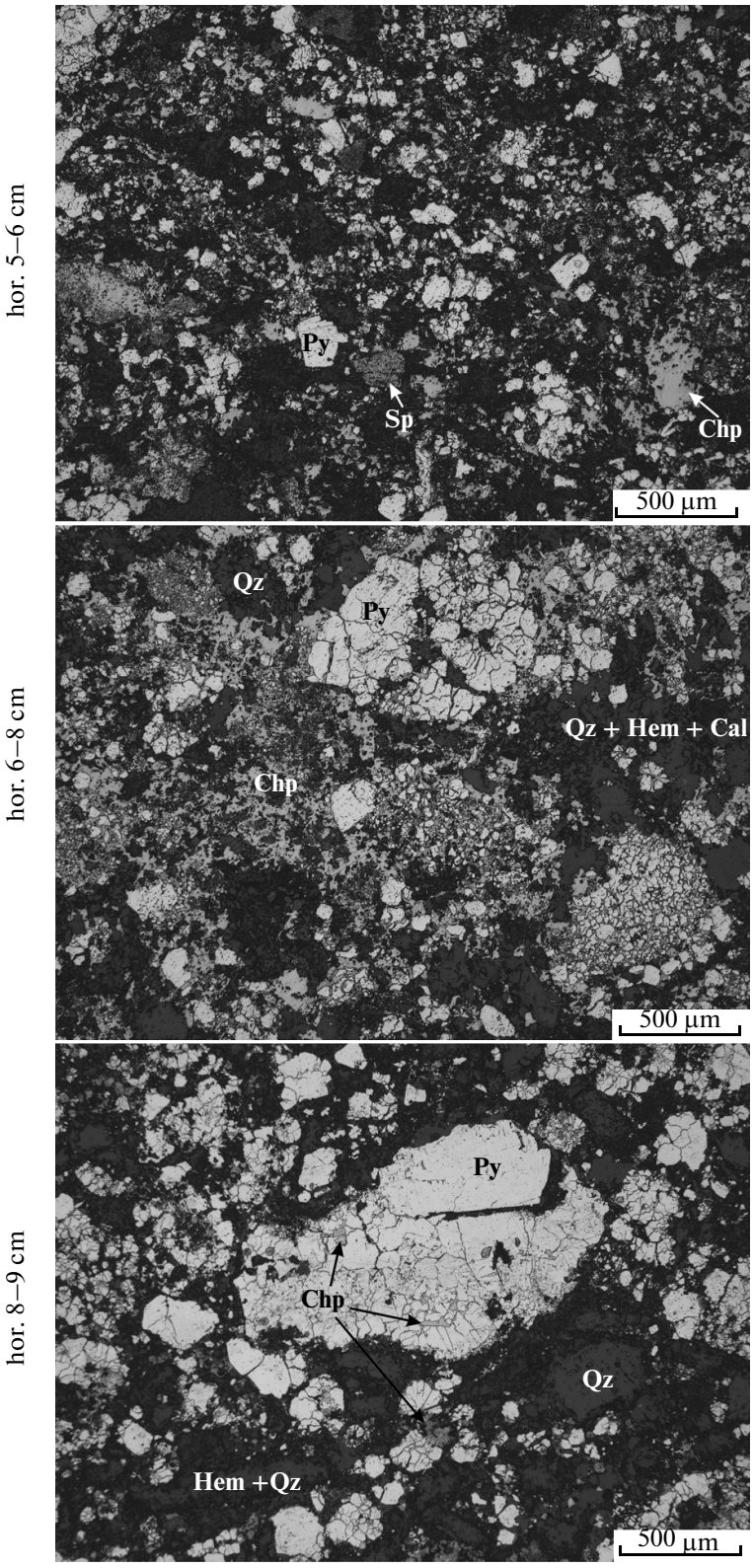

Fig. 5. Microscopic images of distal ore clastic turbidite (sample 3).

All photomicrographs are shown at the same scale in a vertical succession; horizons are indicated to the left. An overall coarsening trend is seen in the ore clasts from top to bottom of the turbidite.

Mineral abbreviations: Py, pyrite; Chp, chalcopyrite; Sp, sphalerite; Qz, quartz; Hem, hematite; and Cal, calcite.

source area. This suggestion is supported by the Fe/Al ratios of gossanites: 13–296 in sample 1, 5–60 in sample 2, and 4–22 in sample 3. Therefore, the lithofacies conditions of accumulation of quartz–hematite sediments in our samples form a continuous sequence toward decreasing Fe (major ore element) and increasing Si and Al (as diluters). In column 32l-362, the Fe/Al ratio is 87.5 for clastic ores and 26–68 for iron hydroxide sediments, suggesting their transitional position in this sequence.

The lowest Fe (20–40 wt %), Si (5–12 wt %), and Al (0.5–4 wt %) contents are characteristic of the ore turbidites, in which Fe is present mostly in sulfide minerals, and Si and Al, in quartz and aluminosilicates, respectively (Table 2). The presence of two horizons (9–11 and 23–25 cm) with anomalous Si content (13.6 wt %) in sample 1 (Table 1) may indicate the additional input of Si to the sediment before lithification. For example, in the Krasnov field (MAR 16°38′ N), the highest amorphous silica content (Si > 10 wt %) was reported from a column closest to the center of the orebody (Rusakov et al., 2011). These conclusions agree with our assumption on the most proximal location of sample 1 to the source area.

Ca–P. The average Ca content of the Devonian samples is not higher than 2.5 wt %, except for intervals 9–11 cm in sample 1 and 6–8 cm in sample 3 (3.6 and 10.0 wt %, respectively) (Table 1). As noted above, Ca occurs mostly as apatite in the gossanites, whereas, in the overlying horizons, it is present as calcite, which is indicated by peaks in the Ca/P curve (shown by the arrow in Fig. 6) and the Ca–P plot (Fig. 7).

The P content is highest in quartz–hematite layers (0.5–1.2 wt % P), where it occurs only in apatite, and lowest in clastic ore layers (<0.3 wt % and mostly <0.05 wt %). Iron hydroxides, the strongest natural sorbents (Rudnicki and Elderfield, 1993) were probably the main source of P in the sediments.

Cu, along with Mn, is the most mobile metal in the sediments studied. Appreciable amounts of Cu were observed in the clastic sulfide layers (>2 wt %), while the Cu content of the gossanites is very low (<0.1 wt %). Copper occurs mainly in chalcopyrite, but is also present as sulfosalts in iron oxide sediments. The precipitation of sulfosalts was probably caused by the deficit of reactive sulfur species in the pore waters of IO- and BIO-type sediments.

Mn. As seen in the diagrams of vertical Mn distribution in the studied sediment sections (Fig. 6), the highest Mn content (>0.1 wt %) was found in quartz–hematite layers within gossanites, except for sample 3, where Mn content in the upper (0–5 cm) gossanite layer is less than 0.05 wt %. The Mn contents of clastic ores are <0.1 wt % and often close to the detection limits of the XRF analyzer. The major Mn minerals in the Devonian–Silurian hydrothermal–sedimentary deposits of the Urals were determined in umbrites, where Mn mainly forms oxide (hausmanite), silicate (braunite, rhodonite, tephroite, and caryopilite), and carbonate (Mn-calcite and rhodochrosite) minerals (Starikova et al., 2004; Maslennikov and Ayupova, 2007). No Mn minerals and significant Mn–Si correlations were identified in our samples. However, a significant correlation between Mn and Al may indicate a link between Mn and aluminosilicates.

Organic Matter

Layers of different mineralogical types show a nonuniform distribution of C_{org} content, which is generally higher in clastic ores than in gossanites and tends to increase with distance from the center of the orebody (hydrothermal vent) (Table 4), and the OI/HI ratio decreases in the same direction. Therefore, with increasing TOC values, the content of hydrocarbons (CH_n) increases with respect to oxygen-containing compounds. This may reflect the increasing proportion of planktonic organic matter from proximal to distal sediments. Previous studies showed that the filamentous Si–Fe aggregates produced by Fe-oxidizing bacteria play a key role in the formation of proximal metalliferous sediments at active hydrothermal fields (Dhillon et al., 2003; Emerson et al., 2007, 2010; Davis and Moyer, 2008; Hodges and Olson, 2009; Rato et al., 2009). These bacteria were shown to be able to oxidize Fe^{2+} to Fe^{3+} and utilize the released energy for CO_2 fixation (Kennedy et al, 2003; Emerson et al., 2007, 2010). The high OI values of the proximal clastic ore (sample 1) may also reflect the predominant role of CO_2 in the activity of microorganisms from habitats in proximity to the center of the orebody.

The carbon isotopic composition of organic matter in sample 1 (Table 4) is close to the average values of Devonian marine sediments, $\delta^{13}C = -(30–26)‰$ PDB (Galimov, 1999). Moreover, well-preserved carbonaceous material from the Early Archean (3240 Ma) Sulphur Springs massive sulfide deposit in the Pilbara block showed almost identical $\delta^{13}C$ values of –(34.0–26.8)‰PDB (Duck et al., 2007). However, it was also noted that this carbon isotopic composition cannot be regarded as a reliable indicator of the sedimentation basin, because it is a product of the destruction of hydrocarbons and proteins accompanied by the enrichment in more stable lipids, lignin, and cellulose (Hoefs, 1980). Therefore, the isotopic composition of organic matter becomes progressively enriched in ^{12}C with increasing geologic age of rocks. The data from sample 3 (without HCl treatment) suggest the predominance of inorganic carbon, as is typical of most sedimentary carbonate rocks. Numerous investigations indicated that the inorganic carbon to organic carbon ratio (C_{carb}/C_{org}) is equal to approximately 4 : 1 and remained almost unchanged over geologic history (Broecker, 1970; Schidlowski et al., 1979). Given the carbon isotopic composition of modern marine carbonates $\delta^{13}C \sim 0‰$, the average isotopic composition of the studied

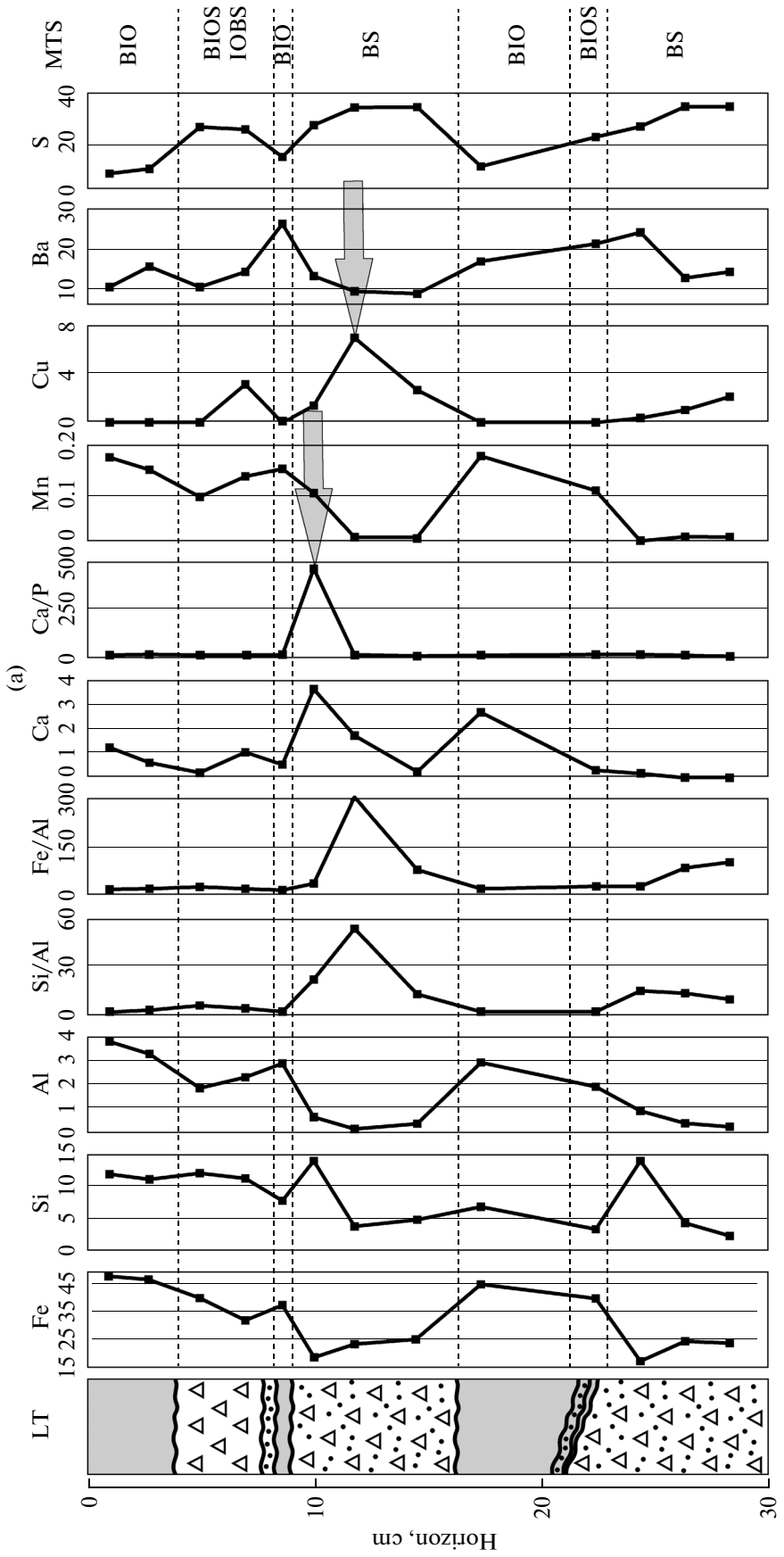

Fig. 6. Vertical distribution of the chemical elements and element ratios across samples (a) 1, (b) 2, and (c) 3; lithotypes (LT): (*1*) gossanite, (*2*) fine-grained clastic ore, (*3*) coarse-grained clastic ore, (*4*) poorly graded clastic ore; mineral types of sediments (MTS): IO—iron oxide, BIO—barite–iron oxide, BIOS—barite–iron oxide–sulfide, IOBS—iron oxide–barite–sulfide, and BS—barite–sulfide. Horizons with the highest calcite and chalcopyrite contents are indicated by arrows.

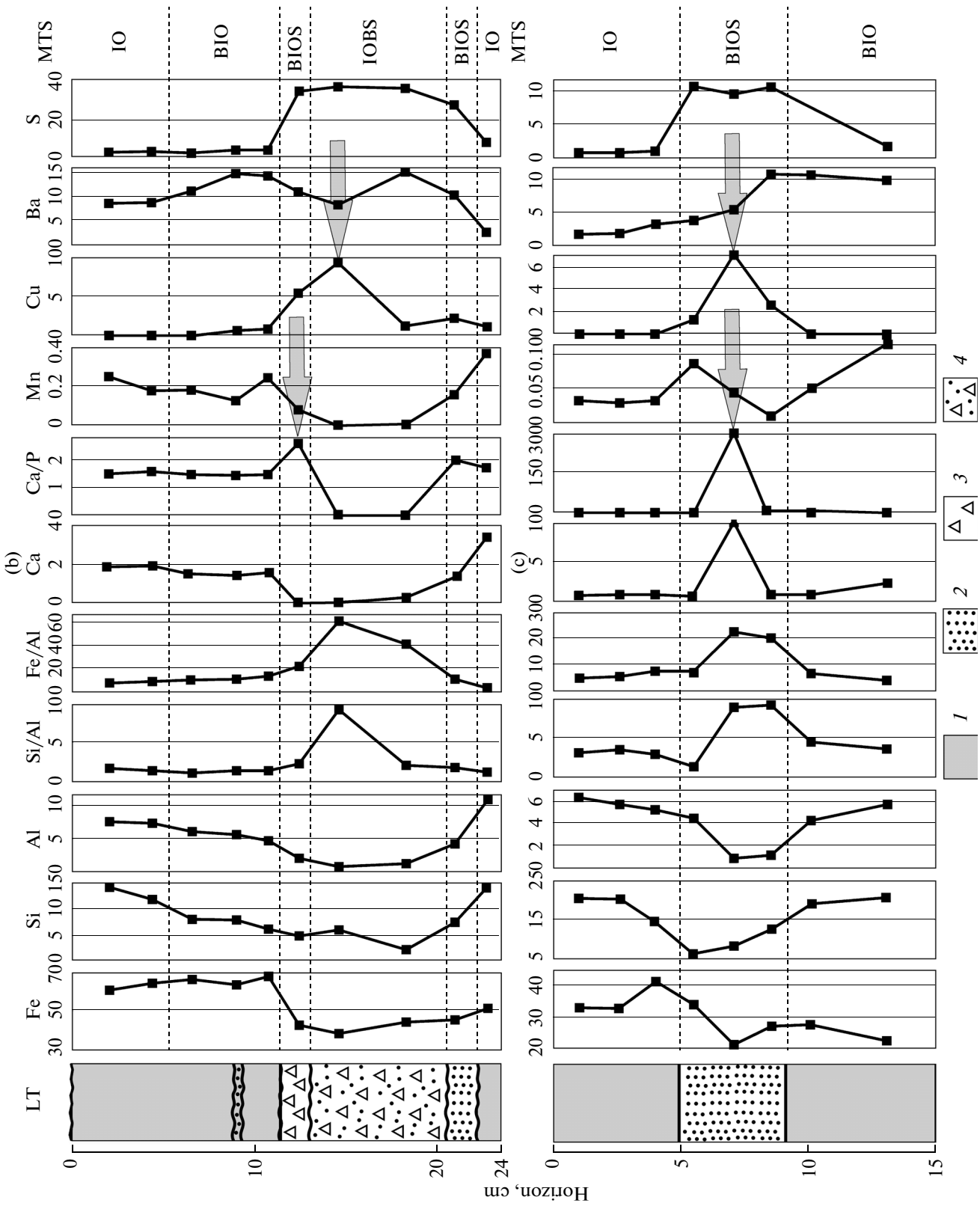
(b)
(c)
MTS
IO
BIO
BIOS
IOBS
BIOS
IO
LT
Fe
Si
Al
Si/Al
Fe/Al
Ca
Ca/P
Mn
Cu
Ba
S
Horizon, cm
0
10
20
24
5
15
1
2
3
4

Fig. 6. (Contd.).

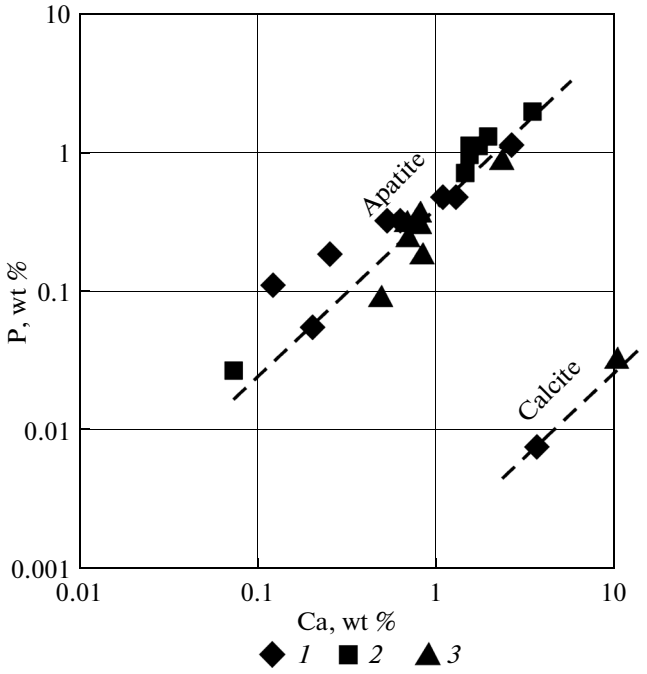

Fig. 7. Ca–P diagram for (*1*) sample 1, (*2*) sample 2, and (*3*) sample 3.

sediments (including carbonates) should be equal to $\delta^{13}C_{bulk} = -(26.93–26.74)/4 \sim -6.7‰$. According to Galimov (1968, 1999), the average isotopic composition of different forms of carbon, considering their mass in the Earth's sedimentary cover, approaches $\delta^{13}C = -5‰$. Both values agree well with our results (Table 4). Moreover, our results are close to the average ($C_{carb} + C_{org}$) composition of marine carbonate sediments, $\delta^{13}C = -(14.7–5.1)‰$ (Ivanov and Lein, 1980). These data may indicate a low degree of carbon isotope fractionation in the sediments studied during the postsedimentary stage.

DISCUSSION

The major mineral compositions of our samples and their modern equivalents (Holocene–Pleistocene) are compared in Table 5. It can be seen that the mineral composition of the quartz–hematite gossanites is poorly correlated with that of iron hydroxide muds of the Semenov hydrothermal cluster. Atacamite is absent in the Devonian sediments. This mineral is associated in sediments with biogenic carbonate material and stable over a narrow range of pH < 8 under strongly oxidizing conditions (at high positive Eh values of >200). In addition, atacamite is unstable at temperatures higher than +(10–13)°C in the carbonate rock–seawater system (Rusakov et al., 2013). Modern sediments are characterized by higher contents of sulfides and barite (SBIH and IHSB types). The absence of their direct equivalents in the rocks of the Molodezhnoe deposit may indicate postsedimentary sulfide oxidation, i.e., the transformation of the SBIH and IHSB types into the BIO type. Compared with modern distal ore clastic sediments (barite–sulfide sand, BSS), their ancient equivalents have higher iron oxide contents; i.e., the BS-type sediments can be transformed into the BIOS and IOBS types owing to oxidizing reactions. This is illustrated by the Cu–S–Fe/4 diagram (Fig. 8). Moreover, the Holocene–Pleistocene sediments of the Semenov hydrothermal cluster have higher Cu contents compared with the sediments of the Molodezhnoe deposit, except for horizon 6–8 cm of sample 3. We suggest that the copper released by the oxidation of primary sulfide minerals is redeposited in other horizons as secondary chalcopyrite. The arrows in Fig. 8b depict the

Table 5. Comparison of major mineral compositions of modern and Devonian ore-bearing hydrothermal sediments

Semenov ore cluster (Rusakov et al., 2013)	Molodezhnoe deposit (this study)	Alteration factor
Atacamite–iron hydroxide (AIH)	Not detected	Atacamite dissolution
Atacamite–barite–iron hydroxide (ABIH)	Not detected	Atacamite dissolution
Iron hydroxide (IH)	Iron oxide (IO)	Dehydration
Barite–iron hydroxide (BIH)	Barite–iron oxide (BIO)	Dehydration
Sulfide–barite–iron hydroxide (SBIH)	Not detected	Sulfide oxidation
Iron hydroxide–sulfide–barite (IHSB)	Not detected	Sulfide oxidation
Not detected (barite–sulfide, BS)	Barite–iron oxide–sulfide (BIOS)	Sulfide oxidation
Not detected (barite–sulfide, BS)	Iron oxide–barite–sulfide (IOBS)	Sulfide oxidation
Barite–sulfide sand (BSS)	Barite–sulfide (BS)	–

* The inferred original composition is shown in parentheses.

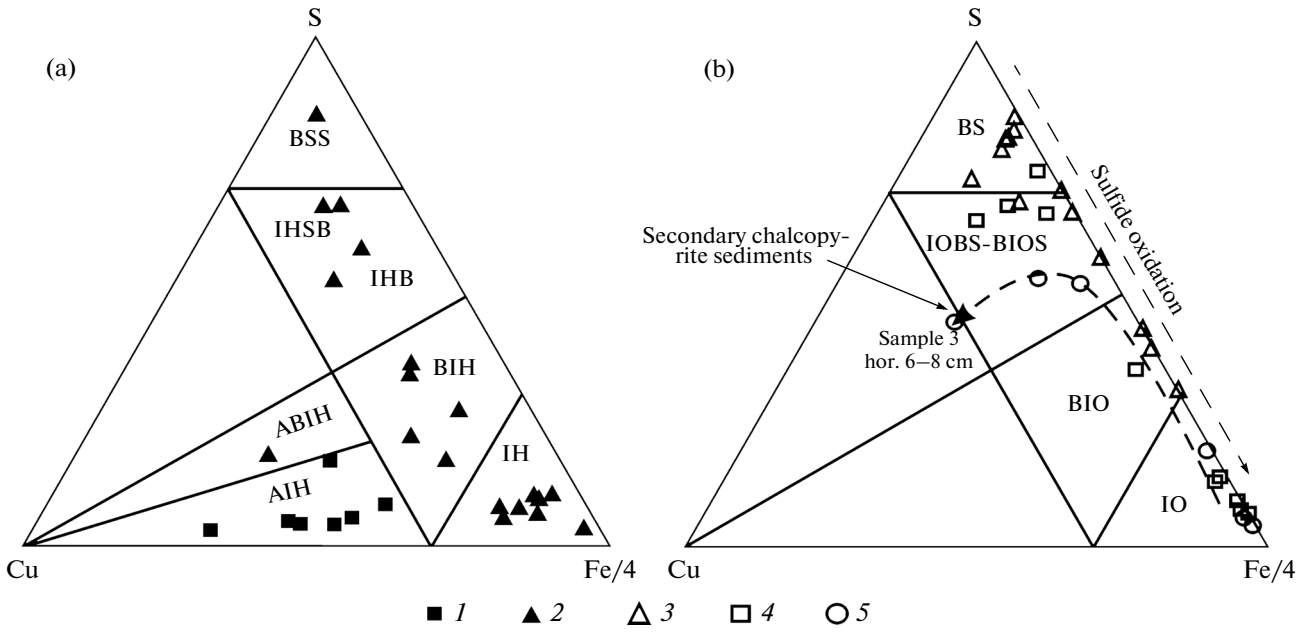

Fig. 8. Cu–S–Fe/4 diagram (wt %) for (a) modern ore-bearing sediments of the Semenov ore cluster (Rusakov et al., 2013) and ore clastic turbidites of the Molodezhnoe massive copper sulfide deposit (this study). (*1–2*) Holocene–Pleistocene sediments: (*1*) Northwestern field and (*2*) Eastern field; (*3–5*) Devonian sediments: (*3*) sample 1, (*4*) sample 2, and (*5*) sample 3. For other explanation, see Table 5 and text.

trend of chemical compositions resulting from the oxidation of sulfides and redeposition of Cu as chalcopyrite in the other horizons. It should be noted that the aforementioned horizon is also strongly enriched in calcite (Table 2).

Since modern sediments were sampled using a box corer suitable for loose sediments, more consolidated coarse-grained ore clastics were not used in our analysis. The latter were sampled using a video-guided grab sampler, which destroys the primary vertical stratification in sediments. The collected sediment is a mixture of ore clasts of different dimensions (from sand-sized particles to rare massive fragments up to ~0.5 m in diameter) and water-rich iron hydroxide muds. Similar ore clastic sediments are also widespread in other hydrothermal fields of the Atlantic Ocean. The visual inspection with a video camera indicates that the surface of these sediments is covered by bacterial mats with numerous living organisms: fishes, eyeless crabs more than 20 cm long, and large carbonate shells of bivalve mollusks (5–10 cm). Part of ore clasts consist of large (*n*10 cm) consolidated fragments of hematitized aggregates.

The above results demonstrate that the Devonian clastic ore turbidites differ from their modern equivalents in (1) the absence of low-temperature mineral assemblages; (2) higher contents of oxidation products in lithified sediments, which reflect the effects of seafloor weathering (halmyrolysis); and (3) sediment dehydration resulting in the replacement of iron hydroxides by hematite and amorphous silica by quartz.

Sedimentation. The presence of clastic ores of different grain sizes and mineralogical types in a single sample suggests that the growing orebody comprised a system of vertical structures (located close to each other), which appeared and collapsed periodically (Figs. 9a, 9b). The collapse of the chimneys was probably caused by the oxidation of sulfides and the destruction of their pyrite matrix due to the infiltration of seawater along fractures into the sulfide mound. This is indicated by the decomposition textures of large pyrite grains in clastic ores. The products of their destruction carried by turbidity flows were deposited at the base of the growing ore mound and interbedded with finely dispersed hydrothermal–sedimentary material (iron hydroxide muds) forming bedded deposits along contacts with massive orebodies.

As shown above, the hydrothermal–sedimentary material and massive sulfides underwent strong oxidizing influence of seawater during the sedimentation stage. This was clearly manifested in the formation of quartz–hematite layers (IO-type sediments). Because of the presence of abundant hematite grains replacing earlier sulfide minerals, these sediments are interpreted to be formed after sulfides. It should be noted, however, that sulfide oxidation products associate with abundant quartz–hematite and hematite–quartz grains produced by the crystallization of Si–Fe and Fe–Si gels of entirely hydrogenous (possibly, biogenic) origin. Previous studies of ore-bearing sediments from the Krasnov and Semenov hydrothermal fields showed that, along with sulfide oxidation products, iron oxyhydroxides in

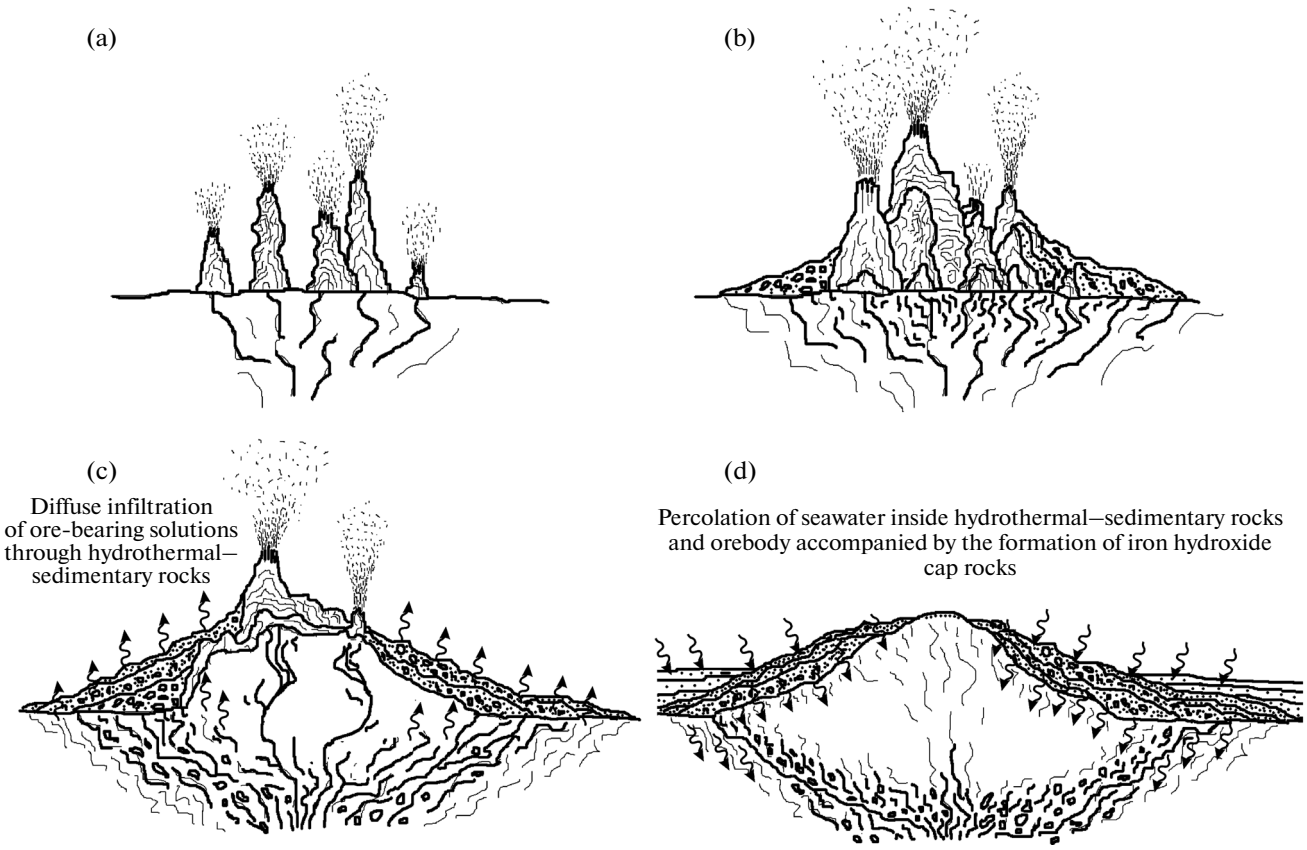

Fig. 9. Main stages of the formation of a hydrothermal orebody and wall rocks of hydrothermal–sedimentary origin during sedimentation and subaqueous diagenetic phases: (a) immature field with isolated ore structures; (b) hydrothermal field at peak hydrothermal activity, the growth of ore structures is accompanied by deposition of ore clastic sediments; (c) mature field with waning hydrothermal activity, copper removal to the outer zone of the ore structure triggers formation of secondary copper minerals in clastic ores (infiltration–metasomatic phase); (d) inactive field where oxidation prevails (infiltration phase).

these sediments may be hydrogenous colloidal X-ray amorphous gels with relatively high Si contents (Rusakov et al., 2011, 2013). It was shown that a wide range of colloids, including silica particles, may be formed by the interaction of hydrothermal solutions with seawater (Rusakov, 2007).

The rate of sediment accumulation is considered the main mechanism controlling the degree of oxidation. The data on the vertical sections of ore-bearing sedimentary columns[1] from the Semenov field (Rusakov et al., 2013) show that oxidation processes usually affected only the upper sedimentary layers, which were in contact with seawater, whereas the ore clastic turbidite layers were weakly oxidized. Closed-system sulfide oxidation decreases the amount of free oxygen, thus strengthening the reducing properties of the pore solutions in sediments, which in turn enhances the dissolution of biogenic carbonates and transfer of some mobile metals from a solid to an aqueous phase. The preservation of large pyrite grains also indicates reducing conditions in the turbidite layers. Therefore, these sediments were deposited as alternating layers with different Eh–pH conditions (oxidizing conditions in the IO-type sediments and reducing conditions in the BS-type ore clastic turbidites).

Secondary minerals (authigenesis). The accumulation of secondary chalcopyrite reflects the postsedimentary effects of copper-bearing solutions on the sediments studied. There are at least two possible mechanisms of formation of secondary copper minerals in this type of deposits. The first mechanism is infiltration metasomatism involving the effect of ascending diffuse flows of hydrothermal solutions. As opposed to the jet flow, the boundary of the diffuse flow may be a continuous front line, which travels upsection without destroying the primary stratification of sediments (Fig. 9c). The second mechanism involves copper leaching from sulfides owing to the infiltration of cold oxidizing seawater into the porous sulfide matrix. Seawater penetrates into an orebody or metalliferous sediments and reacts with sulfide minerals (Fig. 9d). As a result of this reaction, sulfide is converted to hydroxide (Nordstorm, 1982), $(Me)S_n \rightarrow Fe(OH)_3$, while copper and part of

[1] Ore-bearing sediments are defined here as metalliferous sediments with high contents of Cu and Zn, Cu + Zn > 0.25 wt %, when recalculated to carbonate-free material (Beltenev et al., 2006).

iron are released as chlorides into the solution. The influence of both mechanisms on secondary mineral formation has been described in detail using the Semenov field as an example (Rusakov et al., 2013). It should be noted that, at a certain stage of the evolution of a hydrothermal recirculation system, the hydrothermal discharge becomes focused at the center of a sulfide mound and then continues to diffuse and wanes. At this phase, the influence of diffuse discharge gradually gives way to the processes of oxidation; i.e., the infiltration–metasomatic replacement of minerals is changed by the infiltration mechanism.

The mechanism of *infiltration–metasomatic* replacement was considered using the composition of a massive copper sulfide ore (MCS) as an example. The mineral and chemical composition of the ore is given in Tables 1 and 2. Fluid inclusion data and homogenization temperature values show that all fluid inclusions observed in this ore sample were homogeneous liquid and have homogenization temperatures of 150–210°C (Table 3). Massive copper sulfide ores showed higher homogenization temperatures of 150–325°C (Karpukhina et al., 2013). The major mineral composition of a massive copper sulfide ore collected from the Molodezhnoe deposit (Table 2) shows that the ore contains relic pyrite (29.66 wt %) exhibiting decomposition textures, aluminosilicates (1.25 wt %), detrital quartz (1.07 wt %), and separate barite grains (0.14 wt %). This suggests that the chalcopyrite was formed in the MCS after preexisting ore clasts by diffuse infiltration of copper-bearing solutions (infiltration metasomatism). The chlorite could be formed in situ by direct precipitation from hydrothermal solutions or recrystallization of earlier aluminosilicates (including clay minerals). Aluminosilicates are represented in this sample by iron–magnesium phyllosilicate dendrites growing within chalcopyrite, which supports the possibility of clay aluminosilicate formation within the orebody under the influence of high-temperature hydrothermal fluids. However, at the periphery of the orebody, where the infiltration–metasomatic effects of ascending ore-bearing fluids is minimal, reduction diagenesis closely associated with the formation of secondary sulfide minerals and dissolution of biogenic carbonates and manganese oxide minerals should play a key role in the formation of secondary minerals.

In order to reconstruct the *infiltration mechanism* of mineral formation, we performed computer modeling using the HCh (Hydrochemistry) program of Yu.V. Shvarov to compare the equilibrium mineral phases at different temperatures and O_2 partial pressures (Fig. 10). The model system included the following minerals: azurite, native copper, ankerite, anhydrite, apatite, barite, bornite, brucite, chalcocite, chalcopyrite, dolomite, hematite, magnesite, magnetite, muscovite, paragonite, pyrite, quartz, siderite, calcite, sphalerite, tenorite, and troilite, and some mineral assemblages formed by them. The temperature range of 150–400°C was determined from the homogenization temperatures of fluid inclusions in the samples (Table 3) and from studies of geochemical and metasomatic haloes at the mineral deposit (Baranov, 1987).

The results of computer modeling for the BS-type deposits show that the barite–chalcopyrite–pyrite assemblage is stable within the specified temperature range and over a wide range of $\log P(O_2)$. However, at temperatures below 300°C, calcite appears in the system. As noted above, the pore space (interstices) of turbidites were filled with calcite (cement) at the postsedimentary stage. The $\delta^{13}C$ values (Table 4) suggest that calcite was derived from biogenic carbonates, which were supplied to sediments at the sedimentation stage. It is well known that the process of lithification often involves carbonate redistribution between individual layers of sediments (Gavrilov, 1982) as a result of carbon dioxide removal from the system owing to the interaction between CO_2, H_2O, and $CaCO_3$:

$$Ca(HCO_3)_2 \leftrightarrow CO_2\uparrow + H_2O + CaCO_3\downarrow. \quad (1)$$

Since calcium bicarbonate is more soluble than carbonate, the reaction will proceed from right to left.

The modeling for the BIOS-type deposits showed that siderite is formed in the hematite–barite–chalcopyrite–pyrite assemblage at temperatures below 250°C and is joined by calcite below 200°C. The parameters of the replacement of pyrite by chalcopyrite, pyrite by siderite, chalcopyrite by siderite, and siderite by calcite can be calculated from reactions (2)–(5).

$$FeS_2(\text{pyrite}) + 0.5H_2O + CuCl_2^- (aq) = CuFeS_2(\text{chalcopyrite}) + H^+ + 2Cl^- + 0.25O_2(g); \quad (2)$$

$$\log K_2 = \log aH^+ + 2\log aCl^- + 0.25\log fO_2 - \log aCuCl_2^-.$$

Figure 10 shows that all mineral types of sediments contain pyrite coexisting with chalcopyrite.

$$FeS_2(\text{pyrite}) + 2H_2O + CO_2(aq) = FeCO_3(\text{siderite}) + 2H_2S(aq) + 0.5O_2(g), \quad (3)$$

$$\log K_3 = 2\log aH_2S(aq) + 0.5\log fO_2 - \log aCO_2(aq),$$

$$CuFeS_2(\text{chalcopyrite}) + 1.5H_2O + CO_2(aq) + H^+ = FeCO_3(\text{siderit}) + 2H_2S(aq) + Cu^+ + 0.25O_2(g),$$

$$\log K_4 = 2\log aH_2S(aq) + \log aCu^+ + 0.5\log fO_2 - \log aCO_2(aq) + pH. \quad (4)$$

The formation of siderite after pyrite depends not only on the partial pressure of oxygen, $P(O_2)$, but also on the concentration (activity) ratios of dissolved H_2S and CO_2. The formation of siderite after chalcopyrite also depends on copper concentration (Cu^+ activity). The results of modeling show that these reactions proceed at temperatures below 250°C.

$$FeCO_3(\text{siderit}) + Ca^{2+} = CaCO_3(\text{calcite}) + Fe^{2+}, \quad (5)$$

$$\log K_5 = \log aFe^{2+} - (\log aCa^{2+}).$$

The replacement of siderite by calcite requires that $\log aFe^{2+} \le \log aCa^{2+}$. As seen in Fig. 10, at the given oxygen fugacity, the assemblage calcite + siderite does not form in the BIOS-type deposits. Therefore, it can

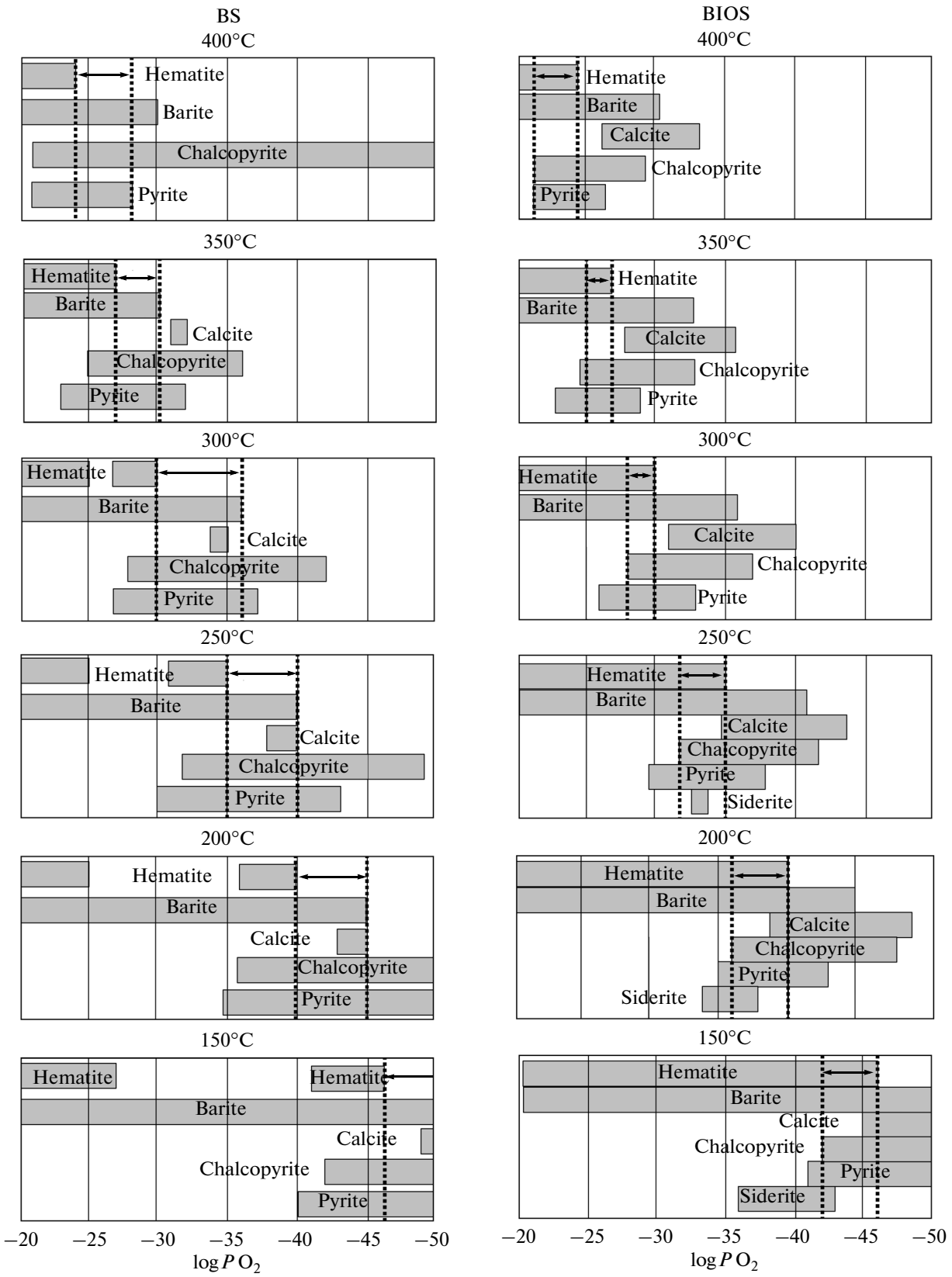

Fig. 10. Stability fields of minerals in the identified MTS (Table 2) at different temperatures and oxygen partial pressures. The stability ranges of mineral assemblages are shown by arrows.

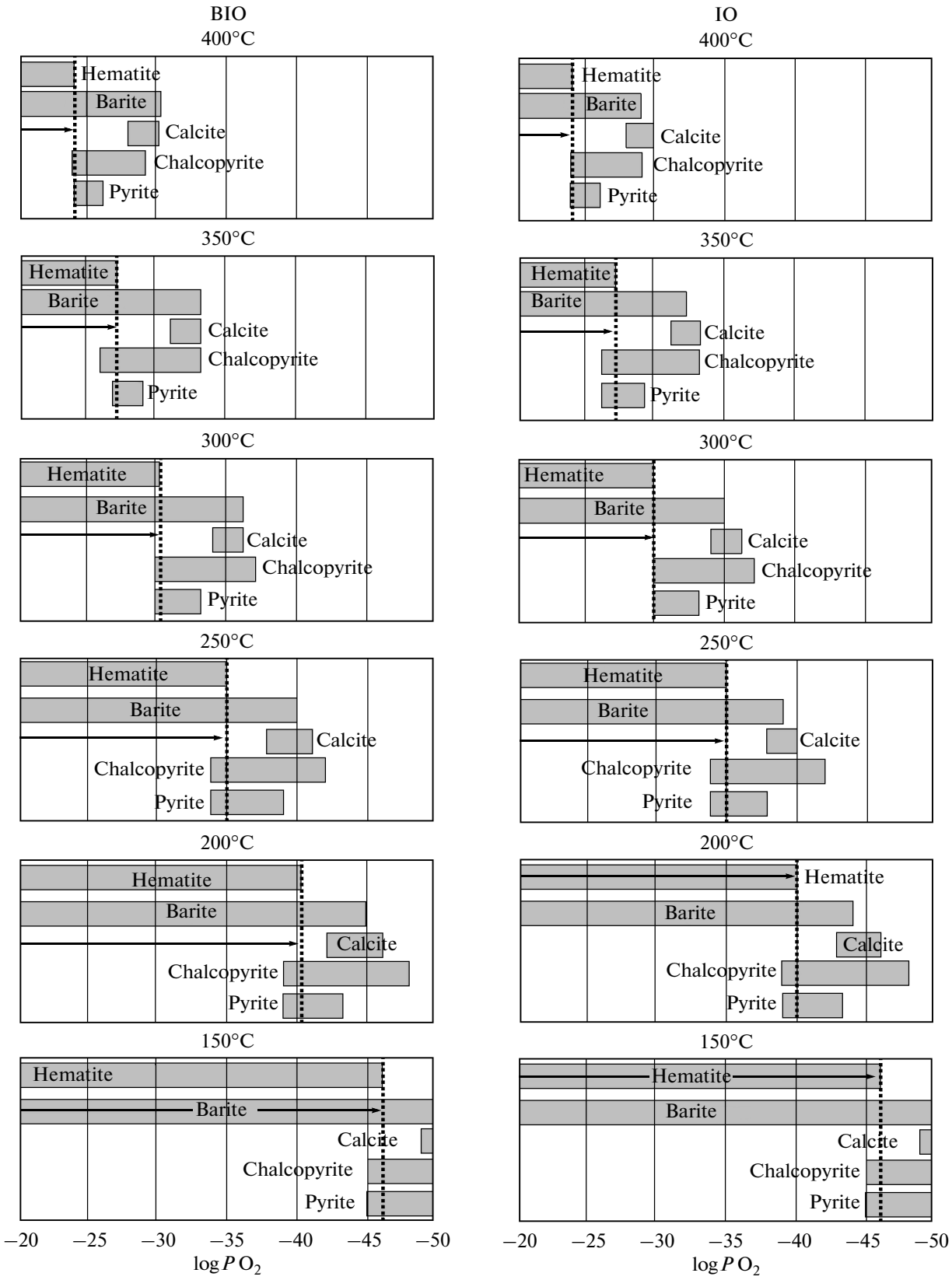
BIO
IO
400°C
350°C
300°C
250°C
200°C
150°C
Hematite
Barite
Calcite
Chalcopyrite
Pyrite
−20 −25 −30 −35 −40 −45 −50
log P O2

Fig. 10. (Contd.).

be concluded that calcite found in association with siderite at 6–8 cm in the BIOS-type deposits of sample 3 is thermodynamically nonequilibrium, i.e., unstable at the given conditions. This result provides additional support that calcite was formed by reaction (1) at a later stage of rock formation.

BIO and ***IO*** types of deposits are also formed at all temperatures and oxygen fugacities considered above (Fig. 10). However, the formation of the IO mineral association (with minor amounts of barite and sulfide minerals) appears more likely at temperatures below 250°C and at $\log P(O_2)$ typical of oxidizing conditions: -33.5 ± 0.5 (250°C), -39.5 ± 0.5 (200°C), and -44.5 ± 0.5 (150°C). It is noteworthy that calcite is absent in this association.

Therefore, the identified mineral associations and the thermodynamic modeling of the stability of these minerals suggest that the formation of secondary minerals involved at least two stages. The first stage included the replacement of pyrite by chalcopyrite (2) and chalcopyrite by siderite (4). The second stage involved carbonate redistribution between individual layers of rocks at lower oxygen activity. Biogenic carbonates were dissolved in the IO- and BIO-type rocks and redeposited in the BIOS- and BS-type rocks as authigenic calcite according to reaction (1).

Lithification. Subsequent lithification of such sediments was probably triggered by the crystallization of iron hydroxides and silica[2], which can be expressed by the hydration–dehydration reactions catalyzed by OH^-:

$$2Fe(OH)_3 \leftrightarrow Fe_2O_3 + 3H_2O, \quad (6)$$

$$(SiO_2)_{x-1} + Si(OH)_4 \leftrightarrow (SiO_2)_x + 2H_2O. \quad (7)$$

The mechanisms of silica crystallization are in turn controlled by a complex interaction between a solid phase of the sediment and pore solutions. It is known that the addition of a salt of a polyvalent metal to a silicate solution results in precipitation of a metal silicate. In the precipitate, silicate ions can be linked together to form an insoluble compound. The study of the mechanisms of chemical precipitation of silica (Iler, 1979) showed that the addition of small amounts of $Fe(OH)_3$ or $Al(OH)_3$, as well as Mn or Mg in a suspended form to a solution of a silicate results in the formation of quartz crystals at low temperatures. The metal hydroxides significantly lower the solubility of silicates, such that quartz becomes a crystallizing phase. Aluminum in this case is the most effective precipitator.

Clay minerals. Studies of metalliferous sediments from modern hydrothermal fields of mid-ocean ridges confirmed the possibility of clay mineral synthesis either by the reaction between hydrothermal fluids and volcanic rocks and sediments or as a result of direct precipitation from hydrothermal fluids mixed with seawater. It was also shown that modern hydrothermal sediments contain not only hydrothermal alteration products of volcanic rocks, such as serpentine, talc, and chlorites (Dias and Barriga, 2006; Dias et al., 2011; Peng et al., 2011), but also muscovite, illite (hydromuscovite), and montmorillonite (smectite and its iron-rich variety, nontronite) (Cole, 1983, 1985, 1988; Kohler et al., 1994; Iizasa et al., 1998; Taitel-Goldman and Singer, 2001a, 2001b; Benjamin and Haymon, 2006; Bentabol et al., 2006; Lackschewitz et al., 2006; Dekov et al., 2007, 2008; Higashi et al, 2007; Hrischeva and Scott, 2007; Augustin et al., 2008; Lantenois et al., 2008; Sun et al., 2012). Dekov et al. (2007) argued that the composition of clay minerals is independent of the type (subtype) of the hydrothermal system and controlled by temperature and the proportion of seawater and hydrothermal fluid in the parental solution. The latter control is characterized by the activity of $Si(OH)_4$ and Mg/Al ratio. It was shown that talc and kerolite–smectite are higher temperature (>250°C) phases, Mg phyllosilicates of the montmorillonite (smectite) group are moderate-temperature (200–250°C) phases, and chlorite and chlorite–smectite are lower temperature (150–200°C) phases.

Furthermore, the possibility of clay mineral synthesis within sediment cannot be ruled out. Sun et al. (2012) described two possible mechanisms of formation of nontronite clays. They may form by precipitation from hydrothermal fluids during their mixing with seawater or by replacement (crystallization) of Fe–Si oxides (gels) directly within the sediment as a result of diffuse percolation of hydrothermal solutions. The former mechanism is exemplified by sediments from the Mariner field of the Valu Fa Ridge, and the latter mechanism, by sediments from the Hine Hina field located in the Lau Basin, in the southern Valu Fa Ridge. Dekov et al. (2008) supposed that the predominance of filamentous nontronite aggregates in the hydrothermal sediments at the Tyrrhenian seafloor is indicative of bacteria-assisted formation. As noted above, subsequent diagenetic changes are associated with the replacement of nontronite by other minerals.

Our data show that the sediments are characterized by the monomineralic composition of aluminosilicates represented entirely by chlorite. Several possible paths of clay mineral alteration during diagenesis and catagenesis have been described in the literature; all of them involve a gradual transformation of disordered mixed-layer minerals to simple ordered minerals via ordered mixed-layer species. For example, Logvinenko and Orlova (1987) showed that, depending on the predominance of a particular chemical element in the system, the clay minerals could be sequentially transformed into chlorite (Mg predominance) or illite (K predominance). Therefore, it can be assumed that the high initial Mg content of pore solutions in metalliferous sediments was due to Mg uptake from seawater. The relatively high loss on ignition values may indirectly

[2] "Silica" is used as a short convenient designation for "silicon dioxide" in all its crystalline, amorphous, and hydrated or hydroxylated forms (Iler, 1979).

indicate high initial water contents in the sediments (LOI = 9.5 wt % on average for sample 1 and up to 21 wt % for horizon 25–27 cm) (Table 1).

CONCLUSIONS

(1) The Devonian ore clastic turbidites of the Molodezhnoe copper massive sulfide deposit are equivalents of Holocene–Pleistocene turbidites (grain flow deposits) in hydrothermal fields of the modern ocean.

(2) The formation of the ore clastic turbidites occurred in two stages. The first stage involved the accumulation of ore clastic layers by turbidity currents acting as agents of gravitational transport of destruction products of the orebody over short distances ($n \times 100$ m). The sediments became affected by infiltration–metasomatic processes owing to the percolation of ascending ore-bearing solutions and infiltration processes owing to the downward movement of seawater. The second stage involved postsedimentary lithification of the sediments, which was accompanied by dehydration, increase in the proportion of oxide minerals, disappearance of temperature-sensitive minerals (atacamite), and transformation of clay minerals.

ACKNOWLEDGMENTS

The authors are deeply grateful to V.V. Maslennikov and I.G. Zhukov (Institute of Mineralogy, Ural Branch of the Russian Academy of Sciences) for organizing field trips to copper massive sulfide deposits of the Southern Urals.

This study was supported by the Russian Foundation for Basic Research (project nos. 11-05-91163a-GFEN and 11-05-00412a) and the Ministry of Education and Science of the Russian Federation (State Contract no. 8667).

REFERENCES

N. Augustin, K. S. Lackschewitz, T. Kuhn, and C. W. Devey, "Mineralogical and chemical mass changes in mafic and ultramafic rock from the Logachev hydrothermal field (MAR 15° N)," Marine Geol. **256**, 18–29 (2008).

E. N. Baranov, *Endogenic Geochemical Aureoles of Massive Sulfide Deposits* (Nauka, Moscow, 1987) [in Russian].

V. Beltenev, V. Shilov, Y. Popova, and I. Rozhdestvenskaya, "Geochemical features of sediments at the hydrothermal fields of MAR 13° N," in *Materials of International Conference: Minerals of the Ocean—3. Future Developments* (St. Petersburg, 2006), pp. 28–29.

V. Beltenev, V. Ivanov, I. Rozhdestvenskaya, G. Cherkashov, T. Stepanova, V. Shilov, A. Pertsev, M. Davydov, I. Egorov, I. Melekestseva, E. Narkevsky, and V. Ignatov, "A new hydrothermal field at 13°30′ N on the Mid-Atlantic Ridge," InterRidge News **16**, 9–10 (2007).

V. Beltenev, V. Ivanov, I. Rozhdestvenskaya, G. Cherkashov, T. Stepanova, V. Shilov, M. Davydov, A. Laiba, V. Kaylio, E. Narkevsky, A. Pertsev, I. Dobretzova, A. Gustaytis, Ye. Popova, and C. Evrard, "New data about hydrothermal fields on the Mid-Atlantic Ridge between 11°–14° N: 32nd Cruise of R/V Professor Logachev," InterRidge News **18**, 14–18 (2009a).

V. Beltenev, V. Ivanov, I. Rozhdestvenskaya, G. Cherkashov, T. Stepanova, V. Shilov, A. Pertsev, M. Davydov, I. Egorov, I. Melekestseva, E. Narkevsky, and V. Ignatov, "New data about structure of hydrothermal fields in the area of 13°31′ N (Semyenov ore cluster)," in *Materials of the XVIII School on Marine Geology "Geology of Seas and Oceans"* (GEOS, Moscow, 2009b), Vol. 2, 133–136.

S. B. Benjamin and R. M. Haymon, "Hydrothermal mineral deposits and fossil biota from a young (0.1 Ma) abyssal hill on the flank of the fast spreading East Pacific Rise: evidence for pulsed hydrothermal flow and tectonic tapping of axial heat and fluids," Geochem., Geophys., Geosyst. **7** (2006). Q05002. doi:10.1029/2005GC001011.

M. Bentabol, M. D. R. Cruz, F. J. Huertas, and J. Linares, "Chemical and structural variability of illitic phases formed from kaolinite in hydrothermal conditions," Appl. Clay Sci. **32**, 111–124 (2006).

A. G. Betekhtin, F. I. Vol'fson, A. N Zavaritsky, et al. *Main Problems in the Theory of Magmatogenic Ore Deposits* (Akad. Nauk SSSR, Moscow, 1953) [in Russian].

W. P. Binney, "A sedimentological investigation of Maclean channel transported sulfide ores Buchans Geology, Newfoundland," Ed. by R.V. Kirkham, Geol. Assoc. Can. Spec. Pap., No. 86-24, 107–147 (1987).

M. B. Borodaevskaya, D. I. Gorzhevsky, A. I. Krivtsov, G. V. Ruchkin, N. S. Skripchenko, G. A. Tvalchrelidze, and G. F. Yakovlev, *Massive Sulfide Deposits of the World* (Nedra, Moscow, 1979) [in Russian].

W. S. Broecker, "A boundary condition on the evolution of atmospheric oxygen," J. Geophys. Res. **75**, 3553–3557 (1970).

T. G. Cole, "Oxygen isotope geochemistry and origin of smectites in the Atlantis II Deep, Red Sea," Earth Planet. Sci. Lett. **66**, 166–176 (1983).

T. G. Cole, "Composition, oxygen isotope geochemistry, and origin of smectite in the metalliferous sediments of the Bauer Deep, southeast Pacific," Geochim. Cosmochim. Acta **49**, 221–235 (1985).

T. G. Cole, "The nature and origin of smectite in the Atlantis II Deep, Red Sea," Can. Mineral. **26**, 755–763 (1988).

Copper Massive Sulfide Deposits of the Urals: Geological Structure, Ed. by V.A. Prokin, F.P. Buslaev, M.I. Ismagilov, et al. (Ural. Nauchn. Ts. Akad. Nauk SSSR, Sverdlovsk, 1988) [in Russian].

Copper Massive Sulfide Deposits of the Urals: Conditions of Formation, Ed. by V.A. Prokin, I.B. Seravnik, F.P. Buslaev, et al. (Ural. Otd. Ross. Akad. Nauk, Yekaterinburg, 1992) [in Russian].

R. Davis and C. Moyer, "Extreme spatial and temporally variability of hydrothermal microbial mat communities along the Mariana island arc and southern Mariana backarc system," J. Geophys. Res. **113** (B08), S15 (2008).

V. M. Dekov, G. D. Kamenov, J. Stummeyer, M. Thiry, C. Savelli, W. C. Shanks, D. Fortin, E. Kuzmann, and A. Vertes, "Hydrothermal nontronite formation at Eolo

Seamount (Aeolian volcanic arc, Tyrrhenian Sea)," Chem. Geol. **245**, 103–119 (2007).

V. M. Dekov, J. Cuadros, W. C. Shanks, and R. A. Koski, "Deposition of talc–kerolite-smectite–smectite at seafloor hydrothermal vent fields: evidence from mineralogical, geochemical and oxygen isotope studies," Chem. Geol. **247**, 171–194 (2008).

A. L. Dergachev, Extended Abstract of Doctoral Dissertation in Geology and Mineralogy (Moscow State University, Moscow, 2010).

A. L. Dergachev, N. E. Sergeeva, and T. A. Felitsyna, "Ore clasts on the Nikolaevskoe massive sulfide–base metal deposit, Rudnyi Altai," Geol. Rudn. Mestorozhd. **1**, 89–95 (1986).

A. Dhillon, A. Teske, J. Dillon, D. A. Stahl, and M. L. Sogin, "Molecular characterization of sulfate-reducing bacteria in the Guaymas Basin," Appl. Environ. Microbiol. **69**, 2765–2772 (2003).

A. S. Dias and F. J. A. S. Barriga, "Mineralogy and geochemistry of hydrothermal sediments from the serpentinite-hosted Saldanha hydrothermal field (36°34′ N; 33°26′ W) at MAR," Mar. Geol. **225**, 157–175 (2006).

A. S. Dias, G. L. Frueh-Green, S. M. Bernasconi, F. J. A. S. Barriga, and Seahma Cruise Team, Charles Darwin 167 Cruise Team, "Geochemistry and stable isotope constraints on high-temperature activity from sediment cores of the Saldanha hydrothermal field," Mar. Geol. **279**, 128–140 (2011).

L. J. Duck, M. Glikson, S. D. Golding, and R. E. Webb, "Microbial remains and other carbonaceous forms from the 3.24 Ga Sulfur Springs black smoker deposit, Western Australia," Precambrian Res. **154**, 205–220 (2007).

D. Emerson, J. A. Rentz, T. G. Lilburn, R. E. Davis, H. Aldrich, C. Chan, and C. L. Moyer, "A novel lineage of proteobacteria involved in formation of marine Fe-oxidizing microbial mat communities," PloS One **2** (7), 667 (2007). doi:10.1371/journal.pone.0000667.

D. Emerson, E. J. Fleming, and J. M. McBeth, "Iron-oxidizing bacteria: an environmental and genomic perspective," Annu. Rev. Microbiol. **64**, 561–583 (2010).

E. M. Galimov, *Geochemistry of Stable Carbon Isotopes* (Nedra, Moscow, 1968) [in Russian].

E. M. Galimov, "The causes of the global variations of carbon isotopic composition in the biosphere," Geochem. Int. **37** (8), 699–714 (1999).

Yu. O. Gavrilov, *Diagenetic Transformations in Clay Deposits* (Middle Miocene of Eastern Cis-Caucasus) (Nauka, Moscow, 1982) [in Russian].

E. G. Gurvich, *Metalliferous Sediments of the Ocean* (Nauchn. Mir, Moscow, 1998) [in Russian].

S. Higashi, H. Miki, and S. Komarneni, "Mn-smectites: hydrothermal synthesis and characterization," Appl. Clay Sci. **38**, 104–112 (2007).

W. Hodges and J. B. Olson, "Molecular composition of bacterial communities within iron-containing flocculent mats associated with submarine volcanoes along the Kermadec Arc," Appl. Environ. Microbiol. **75**, 1650–1657 (2009).

J. Hoefs, *Stable Isotope Geochemistry*, 2nd Ed. (Springer, New York, 1980).

E. Hrischeva and S. D. Scott, "Geochemistry and morphology of metalliferous sediments and oxyhydroxides from the Endeavour segment, Juan de Fuca Ridge," Geochim. Cosmochim. Acta **71**, 3476–4397 (2007).

K. Iizasa, K. Kawasaki, K. Maeda, T. Matsumoto, N. Saito, and K. Hirai, "Hydrothermal sulfide-bearing Fe–Si oxyhydroxide deposits from the Coriolis Troughs, Vanuatu backarc, southwestern Pacific," Mar. Geol. **145**, 1–21 (1998).

R. Iler, *The Chemistry of Silica* (Wiley, New York, 1979).

M. B. Ivanov and A. Yu. Lein, "Distribution of microorganisms and their role in the diagenetic mineral formation," in *Geochemistry of the Diagenesis of Pacific Sediments (Pacific Profile)* (Nauka, Moscow, 1980), pp. 117–137 [in Russian].

B. Köhler, A. Singer, and P. Stoffers, "Biogenic nontronite from marine white smoker chimneys," Clays Clay Miner. **42**, 689–701 (1994).

V. S. Karpukhina, V. B. Naumov, and I. V. Vikent'ev, "Genesis of massive sulfide deposits in the Verkhneural'sk Ore District, the South Urals, Russia: Evidence for magmatic contribution of metals and fluids," Geol. Ore Dep. **55** (2), 125-143 (2013).

S. Kato, C. Kobayashi, T. Kakegawa, and A. Yamagishi, "Microbial communities in iron–silica-rich microbial mats at deep-sea hydrothermal fields of the Southern Mariana Trough," Environ. Microbiol. **11**, 2094–2111 (2009).

C. B. Kennedy, S. D. Scott, and F. G. Ferris, "Characterization of bacteriogenic iron oxide deposits from Axial Volcano, Juan de Fuca Ridge, north-east Pacific Ocean," Geomicrobiol. J. **20**, 199–214 (2003).

V. A. Koroteev, R. G. Yazeva, V. V. Bochkarev, V. P. Moloshag, A. V. Korovko, and Yu. S. Sheremet'ev, *Geological Position and Composition of the Sulfide Ores of the Saf'yanovskoe Deposit (Middle Urals)* (Inst. Geol. Geokhim. Ural. Otd. Ross. Akad. Nauk, Yekaterinburg, 1997) [in Russian].

K. S. Lackschewitz, R. Botz, D. Garbe-Schönberg, J. Scholten, and P. Stoffers, "Mineralogy and geochemistry of clay samples from active hydrothermal vents of the north coast of Iceland," Mar. Geol. **225**, 177–190 (2006).

S. Lantenois, R. Champallier, J.-M. Beny, and F. Muller, "Hydrothermal synthesis and characterization of dioctahedral smectites: a montmorillonites series," Appl. Clay Sci. **38**, 165–178 (2008).

N. V. Logvinenko and L. V. Orlova, *Formation and Alteration of Sedimentary Rocks on Continent and in Ocean* (Nedra, Leningrad, 1987) [in Russian].

V. V. Maslennikov, *Sedimentogenesis, Halmyrolysis, and Ecology of Sulfide Paleohydrothermal Fields by the Example of the South Urals* (Geotur, Miass, 1999) [in Russian].

V. V. Maslennikov, *Lithogenesis and Formation of Massive Sulfide Deposits* (Inst. Mineral. Ural. Otd. Ross. Akad. Nauk, Miass, 2006) [in Russian].

V. V. Maslennikov and N. R. Ayupova, "Siliceous–ferruginous rocks of the Uzel'ga sulfide field (South Urals)," Litosfera **2**, 106–129 (2007).

V. V. Maslennikov, N. R. Ayupova, R. J. Herrington, L. V. Danyushevskiy, and R. R. Large, "Ferruginous and manganiferous haloes around massive sulfide deposits of the Urals," Ore Geol. Rev. **47**, 5–41 (2012).

D. K. Nordstorm, "Aqueous pyrite oxidation and the consequent formation of secondary minerals," in *Acid Sulphate Weathering: Pedogeochemistry and Relationship to Manipulation of Soil Materials*, Ed. by J.A. Kitrick, D.S. Fanning, and L.R. Hossner (Soil Sci. Soc. Am., Madison, 1982), pp. 37–56.

T. M. Pak and A. L. Dergachev, "Ore clasts of the Ridder–Sokol'noe massive sulfide–base metal deposit, Rudnyi Altai," Vestn. Mosk. Univ., Ser. 4: Geol., No. 1, 77–81 (1993).

X. Peng, J. Li, H. Zhon, Z. Wu, J. Li, S. Chen, and H. Yao, "Characteristics and source of inorganic and organic compounds in the sediments from two hydrothermal fields of the Central Indian and Mid-Atlantic Ridges," J. Asian Earth Sci. **41**, 355–368 (2011).

M. D. Rudnick and H. Elderfield, "A chemical model of the buoyant and neutrally buoyant plume above the TAG vent field, 26 degrees N, Mid-Atlantic Ridge," Geochim. Cosmochim. Acta **57**, 2939–2957 (1993).

V. Yu. Rusakov, "Comparative analysis of the mineral and chemical compositions of black smoker smoke at the TAG and Broken Spur hydrothermal fields, Mid-Atlantic Ridge," Geochem. Int. **45** (7), 698–717 (2007).

V. Yu. Rusakov, V. V. Shilov, I. A. Roshchina, and N. N. Kononkova, "Accumulation history of the metalliferous and ore-bearing sediments of the Krasnov hydrothermal field (MAR 16°38′ N) for the past 80 ka BP: Part I.," Geochem. Int. **49** (12), 1208–1238 (2011).

V. Yu. Rusakov, T. G. Kuz'mina, I. A. Roshchina, and V. V. Shilov, "Accumulation history of the metalliferous and ore-bearing sediments of the Krasnov hydrothermal field (MAR 16°38′ N) for last 80 ka: Part II," Geochem. Int. **50** (3), 246–271 (2012).

V. Yu. Rusakov, V. V. Shilov, B. N. Ryzhenko. I. F. Gablina, I. A. Roshchina, T. G. Kuz'mina, N. N. Kononkova, and I. G. Dobretsova, "Mineralogical and geochemical zoning of sediments at the Semenov Cluster of hydrothermal fields, 13°31′–13°30′ N, Mid-Atlantic Ridge," Geochem. Int. **51** (8), 646–669 (2013).

N. P. Safina and V. V. Maslennikov, "Ore clastites of the Yaman-Kasy and Saf'yanovskoe massive sulfide deposits, Urals," (Ural. Otd. Ross. Akad. Nauk, Miass, 2008) [in Russian].

M. Schidlowski, P. W. U. Appel, R. Eichmann, and C. E. Junge, "Carbon isotope geochemistry of the 3.7×10^9–yr-old Isua sediments, West Greenland: implication for the Archean carbon and oxygen cycles," Geochim. Cosmochim. Acta **43**, 189–199 (1979).

N. S. Skripchenko, *Hydrothermal–Sedimentary Sulfide Ores of Basaltoid Associations* (Nedra, Moscow, 1972) [in Russian].

C. D. Spence, "Volcanogenic features of the Vauze sulfide deposit, Noranda, Quebec," Econ. Geol. **70**, 102–114 (1975).

E. V. Starikova, A. I. Brusnitsyn, and I. G. Zhukov, *Paleohydrothermal Build-Up of the Kyzyl Tash Manganese Deposit, South Urals: Structure, Composition, and Genesis* (Nauka, St. Petersburg, 2004) [in Russian].

Z. Sun, H. Zhou, G. P. Glasby, Q. Yang, X. Yin, J. Li, and Z. Chen, "Formation of Fe–Mn–Si oxide and nontronite in hydrothermal fields on the Valu Fa Ridge, Lau Basin," J. Asian Earth Sci. **43**, 64–76 (2012).

N. Taitel-Goldman and A. Singer, "High-resolution transmission electron microscopy study of newly formed sediments in the Atlantis II Deep, Red Sea," Clays Clay Miner. **49**, 174–182 (2001a).

N. Taitel-Goldman and A. Singer, "Metastable Si–Fe phases in hydrothermal sediments of Atlantis II Deep, Red Sea," Clay Miner. **37**, 235-248 (2001b).

V. V. Zaikov and V. V. Maslennikov, "Near-bottom sulfide buildups on the sulfide deposits of the Urals," Dokl. Akad. Nauk SSSR **293** (1), 181–184 (1987).

V. V. Zaikov, T. N. Shadlun, V. V. Maslennikov, and N. S. Bortnikov, "The Yaman–Kasy sulfide lode (South Urals)—remains of ancient "black smokers" on the floor of the Uralian paleoocean," Geol. Rudn. Mestorozhd. **37** (6), 511–529 (1995).

A. N. Zavaritskii, V. A. Zavaritskii, T. N. Shaldun, V. P. Loginov, A. V. Pek, S. N. Ivanov, and L. G. Kvasha, *Massive Sulfide Deposits of the Urals* (Akad. Nauk SSSR, Moscow, 1950) [in Russian].

Translated by N. Kravets